





Reconciling the conflicting extent of overriding plate deformation before and during megathrust earthquakes in South America, Sunda and northeast Japan

Mario D'Acquisto ^{1,2}, Taco Broerse ¹, Celine P. Marsman ¹ and Rob Govers ¹

¹*Tectonophysics Group, Department of Earth Sciences, Utrecht University, 3584 CS Utrecht, Netherlands. E-mail: m.dacquisto@uu.nl*

²*Currently at: Section 1.1: Space Geodetic Techniques, Department 1: Geodesy, GFZ German Research Centre for Geoscience, Telegrafenberg, Potsdam, Germany*

Accepted 2023 June 12. Received 2023 June 9; in original form 2022 June 1

SUMMARY

We aim to better understand the overriding plate deformation during the megathrust earthquake cycle. We estimate the spatial patterns of interseismic GNSS velocities in South America, Southeast Asia and northern Japan and the associated uncertainties due to variations in network density and observation uncertainties. Interseismic velocities with respect to the overriding plate generally decrease with distance from the trench with a steep gradient up to a 'hurdle', beyond which the gradient is distinctly lower and velocities are small. The hurdle is located 500–1000 km away from the trench for the trench-perpendicular velocity component, and either at the same distance or closer for the trench-parallel component. Significant coseismic displacements were observed beyond these hurdles during the 2010 Maule, 2004 Sumatra–Andaman, and 2011 Tohoku earthquakes. We hypothesize that both the interseismic hurdle and the coseismic response result from a mechanical contrast in the overriding plate. We test our hypothesis using physically consistent, generic, 3-D finite element models of the earthquake cycle. Our models show a response similar to the interseismic and coseismic observations for a compliant near-trench overriding plate and an at least five times stiffer overriding plate beyond the contrast. The model results suggest that hurdles are more prominently expressed in observations near strongly locked megathrusts. Previous studies inferred major tectonic or geological boundaries and seismological contrasts located close to the observed hurdles in the studied overriding plates. The compliance contrast probably results from thermal, compositional and thickness contrasts and might cause the observed focusing of smaller-scale deformation like backthrusting.

Key words: Satellite geodesy; Seismic cycle; Continental margins: convergent; Rheology: crust and lithosphere; Subduction zone processes.

1 INTRODUCTION

The great megathrust earthquakes of the previous decades happened after or during the deployment of continuous geodetic networks. Many studies focused on constraining the coseismic fault slip during these earthquakes by combining geodetic with seismological observations (e.g. Simons *et al.* 2011; Vigny *et al.* 2011). Post-seismic processes like relocking, afterslip and viscoelastic flow started to become apparent in the geodetic measurements shortly after these events and continue today, spawning a rich variety of studies that cast new light on processes and rheological properties.

The first earthquake that revealed the widespread extent of coseismic deformation via satellite geodesy was the M_w 9.2 2004 Sumatra–Andaman earthquake. Remarkably, coseismic displacements were recorded at GNSS stations more than 3000 km away

from the megathrust (Vigny *et al.* 2005). Similarly, GNSS stations far into the South American continent recorded displacement due to the M_w 8.8 2010 Maule (Chile) earthquake as far as 1700 km from the trench (Fig. 1; Pollitz *et al.* 2010). Likewise, Wang *et al.* (2011) observed significant coseismic static offsets up to 2500 km away from the epicentre following the M_w 9.0 2011 Tohoku earthquake.

Strain that has accumulated during interseismic periods (mostly) recovers during large megathrust earthquakes and resulting post-seismic relaxation (e.g. Wang *et al.* 2012) and, in at least some cases, also in slow-slip events (SSEs; e.g. Dixon *et al.* 2014; Protti *et al.* 2014; Voss *et al.* 2017). Several studies have focused on determining the interseismic megathrust locking pattern and correlating it to the coseismic slip pattern (e.g. Moreno *et al.* 2010; Loveless & Meade 2011; Protti *et al.* 2014; Malservisi *et al.* 2015; Nocquet *et al.* 2017). Observed interseismic velocities (relative to a stable

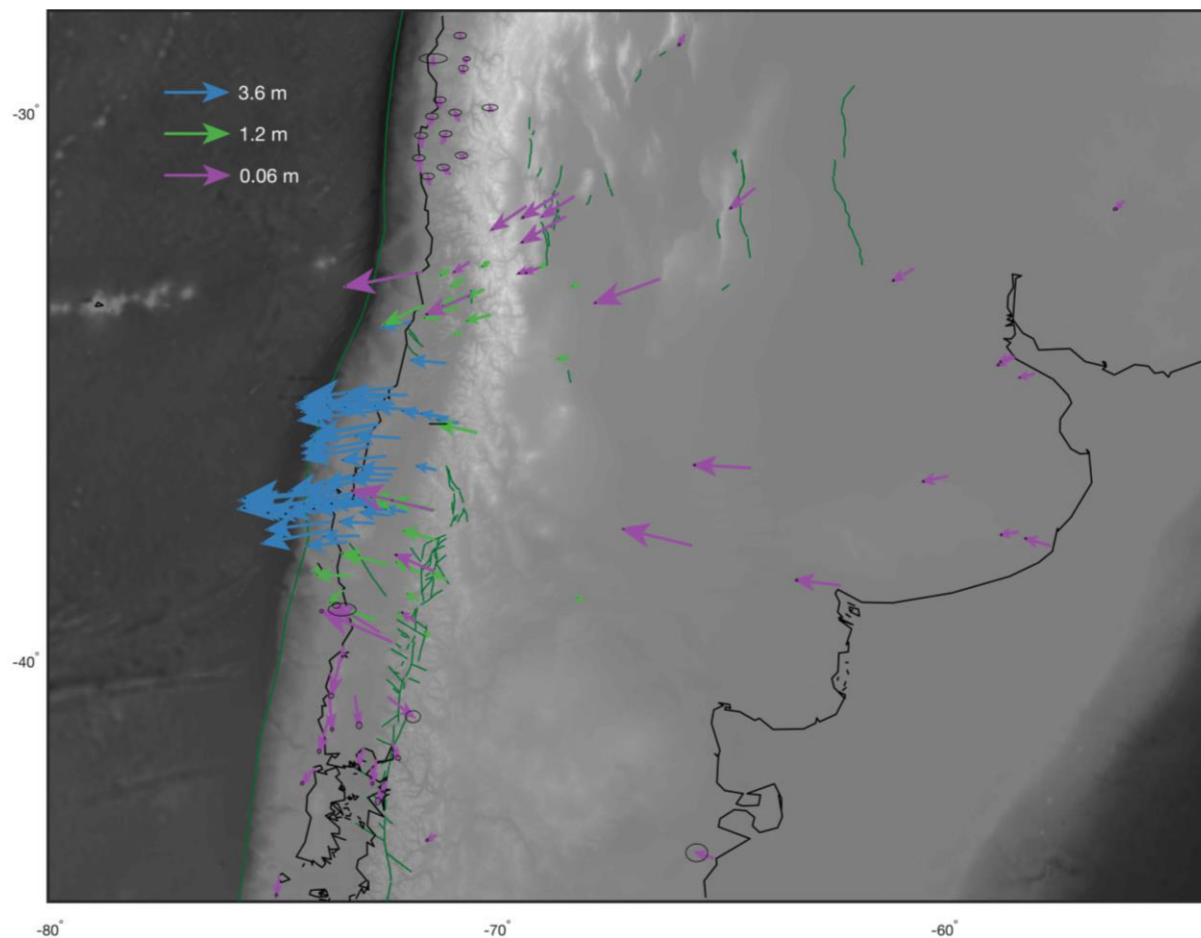


Figure 1. Horizontal coseismic displacements observed at GNSS sites during the 2010 Maule earthquake. Observations are sourced from Delouis *et al.* (2010), Lin *et al.* (2013) Moreno *et al.* (2012), Tong *et al.* (2010) and Vigny *et al.* (2011).

overriding plate reference) are directed landward and decrease with distance from the trench. Interseismic strain buildup seems to focus closer to the margin of the overriding plate, within several hundreds of kilometres from the trench (e.g. Drewes & Heidbach 2012; Simons *et al.* 2007; Kreemer *et al.* 2014; McKenzie & Furlong 2021), compared to deformation due to the largest megathrust earthquakes. In many locations, a distinct break in the slope of the interseismic velocity gradient is observed; from a high velocity gradient near the trench to a small velocity gradient farther away (Brooks *et al.* 2003; Khazaradze & Klotz 2003; Nocquet *et al.* 2014; McFarland *et al.* 2017).

Explanations of the observations vary. The decrease in interseismic velocities with increasing distance from the trench can often be reproduced using a model with a (partly) locked megathrust fault in an elastic half-space (Chlieh *et al.* 2008; Ruegg *et al.* 2009; Liu *et al.* 2010; Métois *et al.* 2012). For parts of the South American Plate, Norabuena *et al.* (1998) pointed out that interseismic strain accumulation is higher farther inland than could be explained by megathrust locking in a fully elastic Earth. Studies focusing on the Central Andes (Norabuena *et al.* 1998; Bevis *et al.* 2001; Brooks *et al.* 2003; McFarland *et al.* 2017; Shi *et al.* 2020) therefore adopted a seismically active backthrust to explain the observed presence of interseismic strain accumulation and of a stable interior beyond the backthrust. Other studies identify slivers or microplates that are bounded by major faults and that are interpreted as decoupled from the rest of the overriding plate, thus deforming and rotating with

respect to the plate interior (Métois *et al.* 2014; Nocquet *et al.* 2014). Both explanations rely on active faults or shear zones, such as backthrusts with a trench-perpendicular length of ~ 200 km (Weiss *et al.* 2016; McFarland *et al.* 2017), that reach deep into the lithosphere and allow near-independent motion of adjacent tectonic domains.

As stated above, interpretations of interseismic strain accumulation are commonly based on fully elastic models, in which overriding plate velocities decrease rapidly with distance from the trench. Post-seismic stress relaxation demonstrates however that the asthenosphere behaves viscoelastically. Models with a viscoelastic asthenosphere rheology predict interseismic velocities that decrease more gradually with distance from the trench compared to elastic models (Wang *et al.* 2012). For increasingly higher asthenospheric viscosities, model results converge to elastic-like behaviour with strain accumulation that is more concentrated in the near-trench region (Trubienko *et al.* 2013; Li *et al.* 2015, 2020; Shi *et al.* 2020). Lower model viscosities result in interseismic velocities that remain significant up to thousands of kilometres into the overriding plate. To match the observed interseismic velocities with their viscoelastic models, Trubienko *et al.* (2013) and Li *et al.* (2015) use long-term (Maxwell) viscosities effectively in the range of $4.0\text{--}5.1 \times 10^{19}$ Pa-s when accounting for the use of plane-strain 2-D models on the relaxation timescale (Melosh & Raefsky 1983). These values are well beyond the high end of the range of estimates of asthenospheric wedge viscosities ($4.0\text{--}10 \times 10^{18}$ Pa-s) from

recent studies of post-seismic viscous relaxation (Hu & Wang 2012; Broerse *et al.* 2015; Klein *et al.* 2016; Li *et al.* 2018; Qiu *et al.* 2018; Agata *et al.* 2019; Muto *et al.* 2019; Fukuda & Johnson 2021; see Section 5.2).

The South American margin has played a significant role in the development of ideas about interseismic strain accumulation because of the presence of an extensive continental plate interior. In other subduction zones, the gradient of interseismic velocities is also observable over a wide distance, although the view is fragmented because of offshore regions with no GNSS observations (Figs 2, 3). Interseismic velocities in Sumatra before the 2004 earthquake show a distinct decrease with distance from the trench (Prawirodirdjo *et al.* 1997; Simons *et al.* 2007), even though the trench-parallel motions are strongly affected by the Sumatran Fault (Genrich *et al.* 2000a). Similarly, landward velocities in northern Honshu (Japan) and Hokkaido, recorded before the 2003 Tokachi and 2011 Tohoku earthquakes (Sagiya *et al.* 2000), show a steep decrease with distance from the trench. More significant difficulties in observing the interseismic velocity gradient arise in other subduction margins like Cascadia, where other tectonic processes overprint the interseismic locking signal, like the Mendocino Crustal Conveyor (Furlong & Govers 1999) and the northward migration of the Sierra Nevada-Great Valley block (Williams *et al.* 2006). In southern Honshu and Shikoku, strain rates due to convergence on the Japan trench and Nankai trench are superimposed, which makes it difficult to isolate the far-field interseismic velocity pattern. As discussed in Govers *et al.* (2018), continental Alaska shows continuing post-seismic relaxation following the 1964 Prince William Sound earthquake. For these reasons, we focus on regions which, although exhibiting tectonic complexities, show identifiable signatures of interplate convergence and megathrust locking and for which data unaffected by post-seismic relaxation are available: South America, Sunda and northern Japan.

In this study, we address the apparently contrasting geodetic observation that interseismic deformation of the overriding plate focuses within several hundreds of kilometres from the trench, whereas coseismic strain release extends over much greater distances. We observe a break in the slope of trench-parallel and trench-perpendicular velocity components as a function of trench distance, which we refer to as a hurdle. Long-lived subduction tectonically accretes blocks and deforms the overriding plate, by an amount that depends on existing lithospheric compliance contrasts (Mouthereau *et al.* 2013; Pearson *et al.* 2013). These compliance contrasts, inherited and resulting from tectonic rejuvenation, remain visible today as significant contrasts in the effective elastic thickness of the lithosphere (Watts 2015) that correlate with tectonic boundaries between different blocks (Watts *et al.* 1995; Stewart & Watts 1997). Convergent deformation, including backthrusts, likely localizes at these naturally occurring contrasts. Here we consider the possibility that these lateral contrasts cause the hurdle-like behaviour of the overriding plate. Because of our context of the earthquake cycle we consider contrasts in elastic properties.

Our study consists of two main elements: mapping the patterns of interseismic velocities, and interpreting interseismic velocity gradients in terms of mechanical contrasts. We characterize the spatial pattern of horizontal interseismic surface motion along the South America Trench, the Sunda Trench and Japan Trench based on available observations (Section 2). Near-trench regions are typically (much) more densely instrumented than intermediate and far-field regions, and interseismic velocities of benchmarks have variable uncertainties. We account for how these factors propagate into uncertainties in the interpolated velocity fields. We estimate

the approximate location of the hurdle, the dominant break in the slope of interseismic velocities, and discuss its significance.

To test our hypothesis that hurdle-like behaviour is related to elastic contrasts in the overriding plate, we construct a 3-D viscoelastic numerical model (Section 3), analyse our model results and their robustness (Section 4). Next, we discuss their significance and possible interpretations in the context of other proposed causes (Section 5). We conclude (Section 6) that a mechanical contrast in the overriding plate, with a more compliant near-trench region and a less compliant far-field region, is a likely candidate for explaining both the interseismic and coseismic observations in the three analysed subduction zones.

2 ANALYSIS OF INTERSEISMIC VELOCITY OBSERVATIONS

2.1 Data selection

We compile previously published horizontal velocities along three convergent margins with abundant interseismic GNSS observations: the Peru–Chile Trench (South America; Kendrick *et al.* 2001; Klotz *et al.* 2001; Brooks *et al.* 2003, 2011; Chlieh *et al.* 2004; Gagnon *et al.* 2005; Ruegg *et al.* 2009; Seemüller *et al.* 2010a; Métivier *et al.* 2012, 2013, 2014; Drewes & Heidbach 2012; Nocquet *et al.* 2014, 2014; Alvarado *et al.* 2014; Blewitt *et al.* 2016; Weiss *et al.* 2016; McFarland *et al.* 2017; Klein *et al.* 2018a), the Sunda Trench (Sumatra and Java, Indonesia; Genrich *et al.* 2000a; Bock *et al.* 2003; Simons *et al.* 2007; Chlieh *et al.* 2008; Prawirodirdjo *et al.* 2010; Kreemer *et al.* 2014; Koulali *et al.* 2017) and the Japan Trench (Sagiya *et al.* 2000; Apel *et al.* 2006a; Jin & Park 2006; Liu *et al.* 2010; Nishimura 2011; Shestakov *et al.* 2011; Ohzono *et al.* 2011; Yoshioka & Matsuoka 2013; Kreemer *et al.* 2014; Freed *et al.* 2017). To prevent contamination by post-seismic velocities that are oceanward and opposite to landward interseismic velocities, we exclude velocities based on observations following significant ($M_w \geq 7.5$) earthquakes in the trench-perpendicular sector of the subduction zone where the megathrust event occurred (see Fig. 2), unless the published velocities were explicitly corrected for post-seismic transients. Please refer to the Tables S1–S3 for more details on the observation period of data sources and possible post-seismic corrections. We use velocities expressed in the global reference frame ITRF (Altamimi *et al.* 2011). For the majority of our data sources we make use of the velocity tables from Kreemer *et al.* (2014), who have estimated a translation rate and rotation rate for each published set of velocities to express velocities in the same IGS08 reference frame (the IGS realization of ITRF2008; Rebischung *et al.* 2012). We feature velocities expressed in ITRF2005, ITRF2008 and ITRF2014; differences resulting from these different realizations are well below the 1 mm yr^{-1} level (Métivier *et al.* 2020). We also include velocities from Weiss *et al.* (2016), which are only provided in a self-determined, non-explicit South America reference frame. However, biases because of different reference frames are small: the mean difference in velocities between those of Weiss and the South America far-field velocities of Blewitt *et al.* (2016) is below 0.2 mm yr^{-1} .

Subsequently, we transform ITRF-expressed velocities to the overriding plate reference. For the sites in South America and Japan we apply the South America and Okhotsk Euler poles, respectively, of Kreemer *et al.* (2014). For Sumatra we make use of the Sunda Euler pole of Simons *et al.* (2007), who identify Sundaland as a

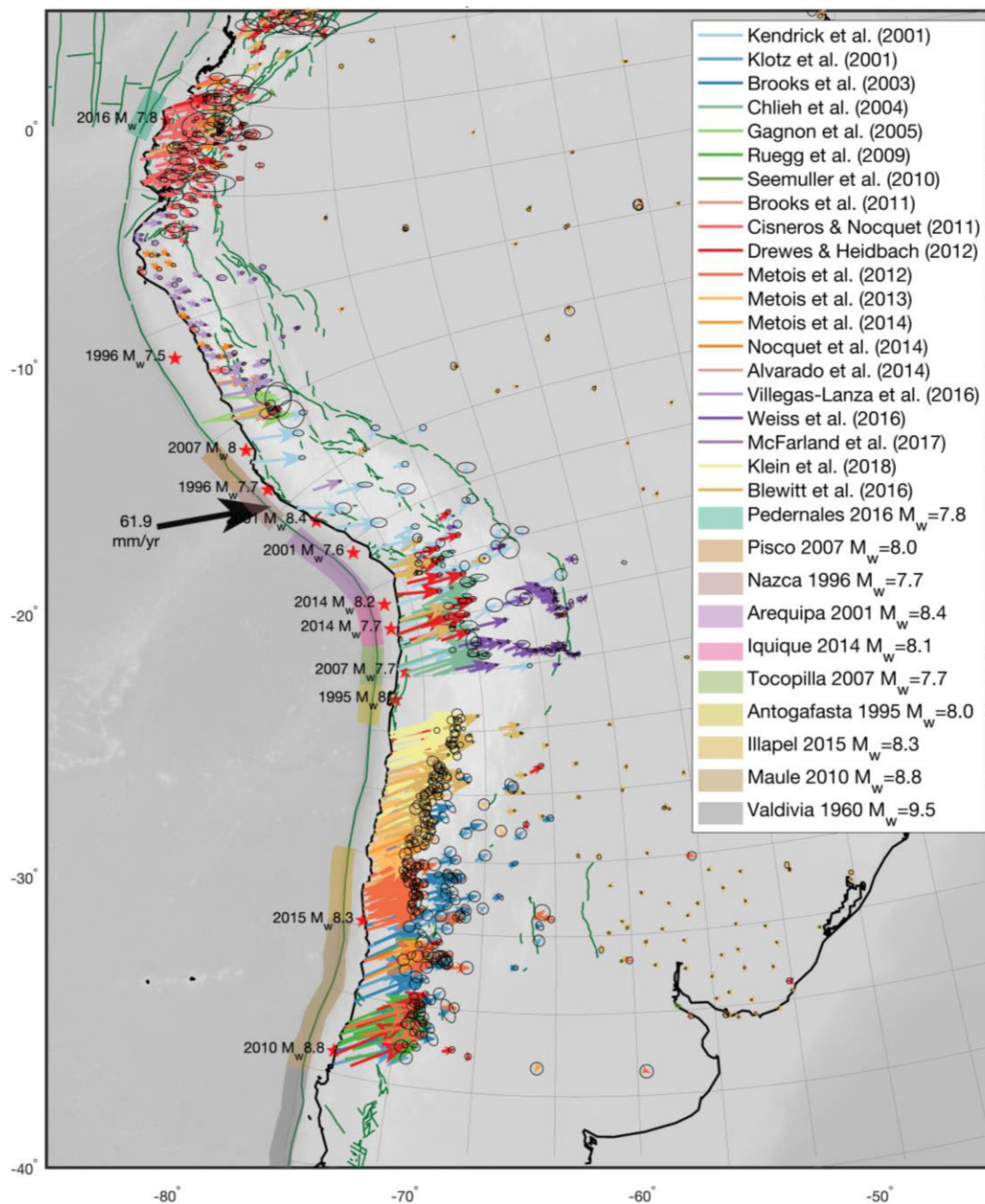


Figure 2. Interseismic GNSS data that we use in our study regions. Panels show published geodetic velocities, coastlines and topography, and active faults in green. Thick black arrows show interplate convergence velocities from Kreemer *et al.* (2014) (South America), Simons *et al.* (2007) (Indonesia) and Kreemer *et al.* (2014) (Japan). Red stars show epicentres of earthquakes ($M_w \geq 7.5$) that affect our data selection as follows. In each segment of the subduction zone that hosted such earthquake, we discard all velocities based on observations taken after the event, unless the velocities have been explicitly corrected for post-seismic transients (see Tables S1–S3). Specifically, we exclude data in the region affected by coseismic displacements and post-seismic transients in the trench-perpendicular area behind the coloured sections of the trench. In South America, we thus exclude all data after the 1995 Antofagasta earthquake, as there is no pre-earthquake GNSS data available. Similarly, we exclude all post-2011 Tohoku data in Japan. Velocities increase towards the west in southwest Hokkaido likely due to post-seismic relaxation after the 1993 Hokkaido Nansei earthquake (Ueda *et al.* 2003), which is why we exclude these data also. We set data exclusion zones stretching from the indicated parts of the trench to a given distance from the trench (1000 and 1500 km for events larger than $M_w \geq 8.7$), which we apply to data collected after the events. Grey lines show the conformal grid that we use to identify trench-perpendicular/parallel directions.

coherent block moving independently of the South China block farther north. More information about data sources is available in Text S1 and Tables S1, S2 and S3. The resultant interseismic velocities, described in a consistent reference frame throughout each studied region, show a clear contrast between high near-trench velocities and a stable interior (Fig. 2).

2.2 Velocity decomposition into trench-perpendicular and -parallel components

We define a conformal projection using a Schwarz-Christoffel map (Driscoll 2002) to identify trench-perpendicular and trench-parallel directions in our study areas. This produces a coordinate system that

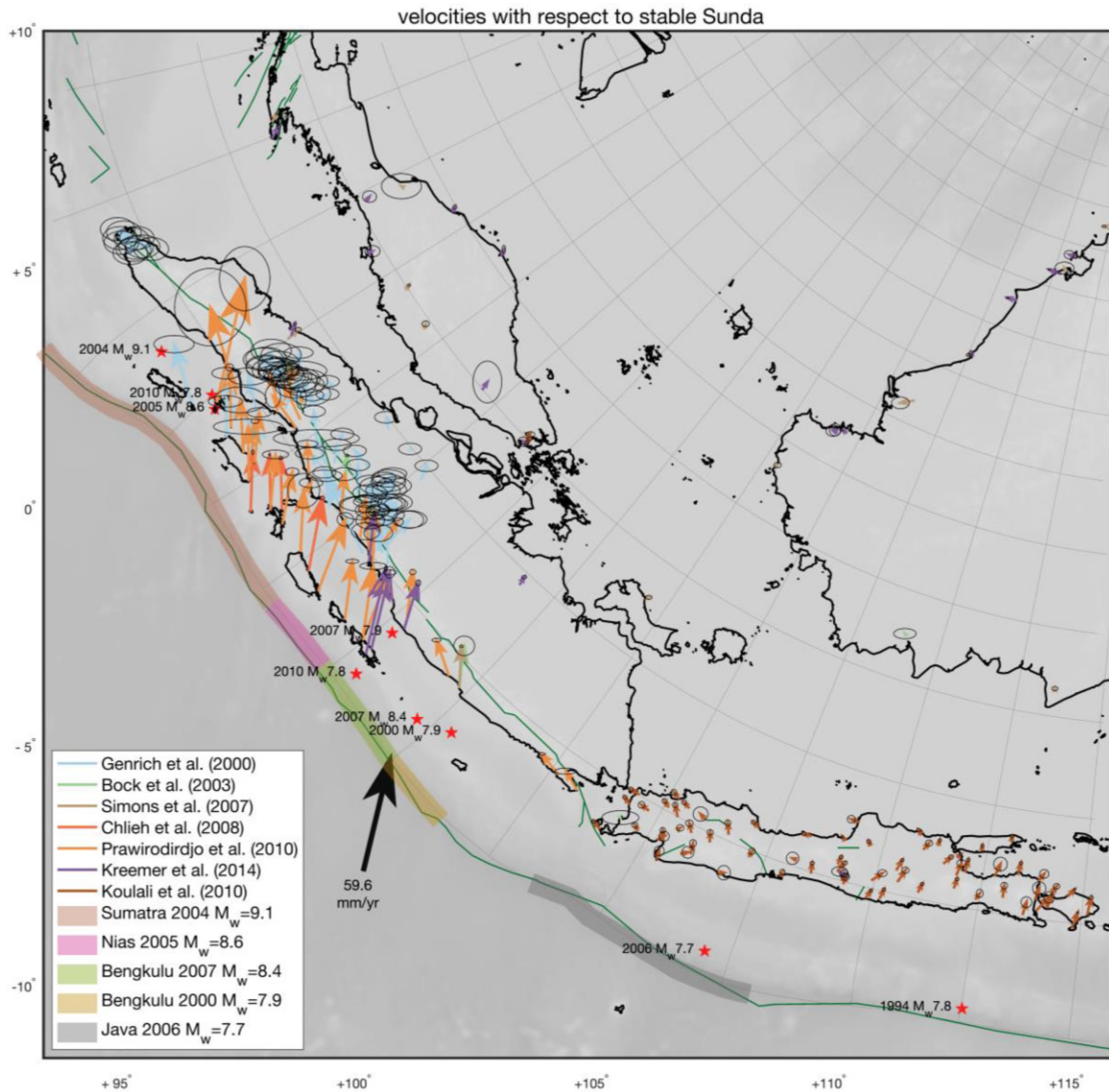


Figure 2. Continued.

smoothly grades, from precisely aligned (parallel and perpendicular) to the trench at the trench, to aligned with the broad regional trend of the trench in the plate interior. From the mathematical mapping of geographical coordinates into local trench-perpendicular and -parallel coordinates we derive the angles between the two orthogonal coordinate systems at an arbitrary location, allowing us to compute the trench-perpendicular and trench-parallel components of each velocity vector. Figs S1–S3 coordinate grid into geographical coordinates (also shown in Fig. 2) and the decomposition of the velocities in locally trench-parallel and trench-perpendicular components.

2.3 Interpolation of the decomposed velocity fields

Most geodetic studies of GNSS interseismic deformation have focused on the deforming zones close to the margin for the purpose of estimating megathrust locking. In most regions, GNSS stations are unevenly distributed, much more densely in near-trench areas than farther away from the trench, in the far-field plate interior that is

used as the stable reference. To obtain homogeneously distributed velocity amplitudes and estimate the location of velocity gradient discontinuities, we separately interpolate the observed trench-perpendicular and trench-parallel velocity components. We account for the propagation of observational uncertainty and for the potential velocity variability in between observation sites in the following way. We interpolate the velocities and estimate uncertainties using ordinary kriging (Wackernagel 2003), a weighted mean method that relies on the statistics of the observed data. The mean, variance and correlation of the velocity field are spatially heterogeneous, so we define natural neighbourhoods to construct correlograms that describe the local variability of the velocity field (Broerse et al., in prep.; Machuca-Mory & Deutsch 2013; Fouedjio & Séguret 2016). We specifically account for the curvature of the Earth in the computation of distances and the choice of covariance models in the kriging procedure. Further technical details are in Text S1 and Figs S1–S12.

The uncertainties we compute for our interpolated velocity field reflect both the uncertainty of velocity observations (i.e. data uncertainty) and the expected variance of the velocity field between

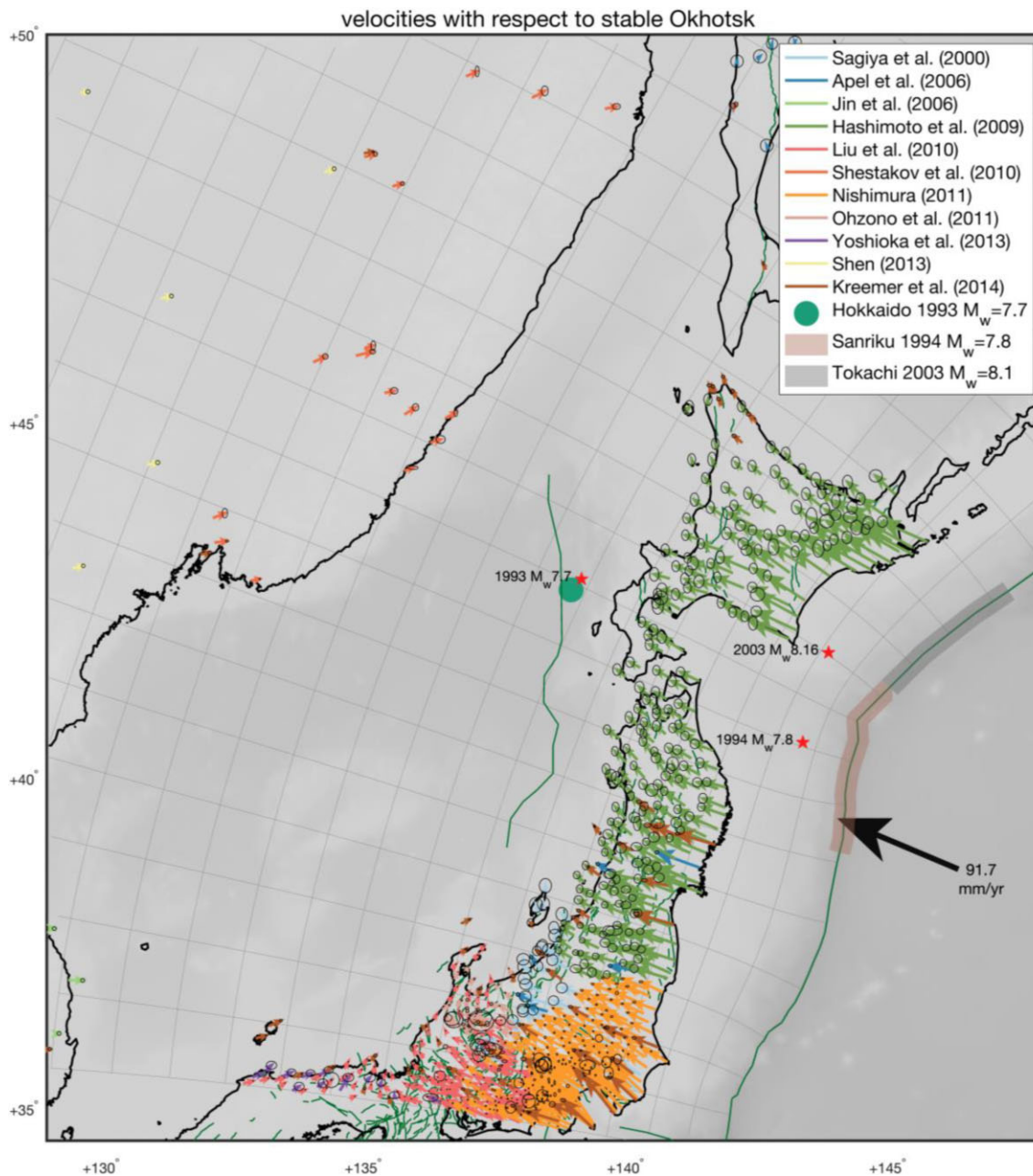


Figure 2. Continued.

observation points. Figs S10–S12 show that uncertainties of the interpolated velocity field are small in regions with little variability in observed velocities, but increase substantially with distance from observation points in regions where observed velocities vary significantly in between observation points.

2.4 Estimation of the hurdle location

The hurdle constitutes the main discontinuity in velocity gradients separating the interseismically deforming margin from the stable interior. We use the gridded interpolated velocity fields together with their uncertainty estimates to estimate the hurdle location as function of distance from the trench. First, we take trench-perpendicular profiles, which are equidistant at the trench, through the 2-D in-

terpolated field, 277 in total for South America, 64 for Sunda and 51 for Japan. Subsequently, we fit a piece-wise continuous function consisting of two linear segments to the velocity as function of distance along the profile. We use weighted non-linear least squares with a Trust Region algorithm, using as weights the inverse of variances from the kriging. The junction between the two segments, located in the fitting process, constitutes the hurdle. We propagate the velocity uncertainties to the uncertainties of the hurdle location, approximated by linearization of the non-linear problem (*cf.* Text S1). Figs 3–5 show maps of our estimated hurdle locations for each of the subduction zones and selected trench-perpendicular profiles of interpolated velocities with their uncertainties, nearby GNSS observations, and hurdle locations.

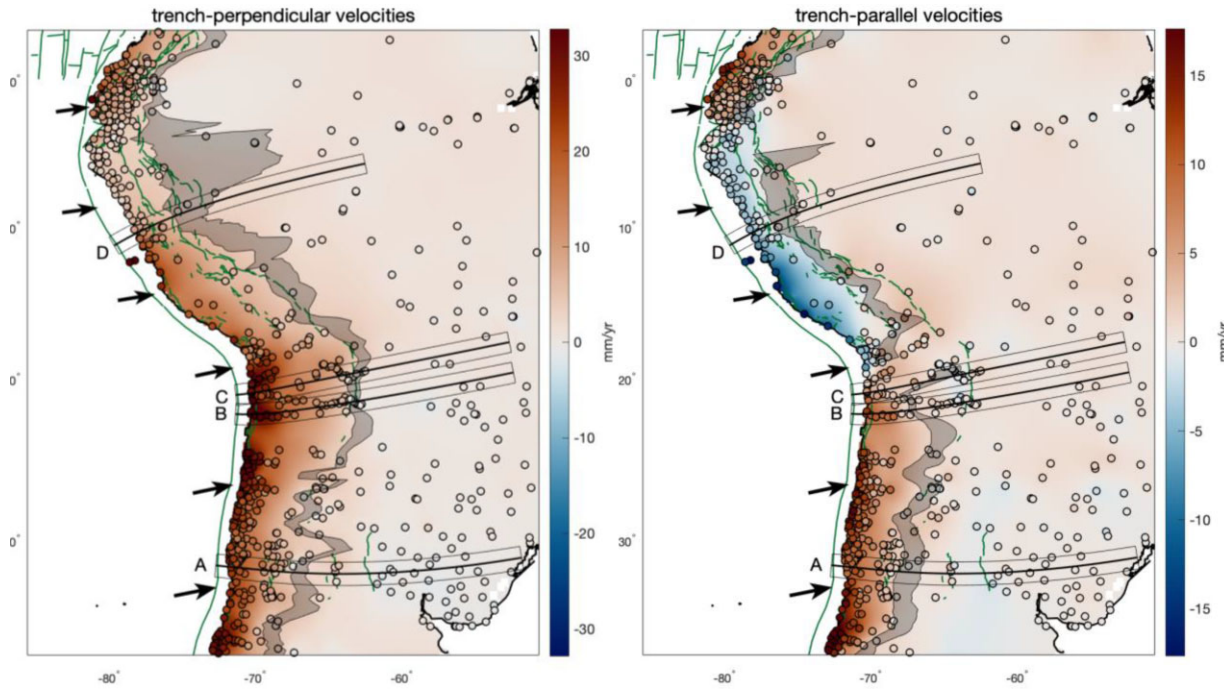


Figure 3. Estimated hurdle locations in South America. The maps show interpolated interseismic velocity components (colours, mm yr^{-1}) and the 95 per cent confidence interval of the location of the hurdle in grey. Active faults (Styron & Pagani 2020) are shown in green; on the left, we show trench-perpendicular velocities (positive landward), and on the right trench-parallel velocities (positive left-lateral). In both map panels, circles represent GNSS station locations, and their fill colour is the observed interseismic velocity component. Arrows show the convergence direction along the Peru–Chile Trench (Kreemer *et al.* 2014). Coastlines are black. Locations of trench-perpendicular swath profile lines A, B and C are shown on the maps by the thick line surrounded by the thinner lines showing the swath width. The panels below show the velocity profiles along A, B and C, including both interpolated velocity components (continuous lines) with 1–standard deviation uncertainty (transparent bands), and the velocity components at GNSS stations within the swath (dots) with 1–standard deviation error bars. Note that the interpolated velocities are based on all GNSS velocity estimates, and not only those shown in the swath for reference. Dotted green and orange lines depict the piece-wise linear fit. Vertical dotted lines and coloured bands outline estimated hurdle distances with 95 per cent confidence intervals. Video S1 shows trench-perpendicular cross-sections along the entire margin.

2.5 Data analysis results

Figs 3–5 show the interpolated velocity fields and hurdle locations, together with velocities along select trench-perpendicular profiles. Additional velocity profiles, all along the three subduction zones, are shown in animations in Videos S1–S3. Both velocity components decrease steeply with distance from the trench up to a hurdle, behind which a far-field region starts with low velocity amplitudes and gradients. The hurdle location can be constrained best when both the velocity uncertainties are small and there exists a strong discontinuity between the near-field and far-field velocity gradient. Trench-perpendicular velocities in particular show a steep near-trench decrease, except above sections of the megathrust that are not locked over an extensive trench-parallel distance. Such unlocked portions of the subduction interface are characterized by low interseismic velocity magnitudes (e.g. Matsu’ura & Sato 1989), for example in northern Peru ($4\text{--}9^\circ\text{S}$; Nocquet *et al.* 2014; Herman & Govers 2020) and Java (Koulali *et al.* 2017). Trench-parallel velocities show a more complex behaviour, particularly where the convergence obliquity changes direction (inverting the sign of near-trench trench-parallel velocities) and forearc slivers have been suggested to exist (Nocquet *et al.* 2014; Métois *et al.* 2016; Herman & Govers 2020). Nevertheless, trench-parallel velocities in South America also generally decrease steeply with distance from the trench and suggest a hurdle, beyond which amplitudes are near-zero and the slope is very shallow (Video S1).

In South America, we can identify the trench-perpendicular hurdle as the location of the transition between rapid near-trench decay and the other, shallower slope in the far-field. Along the margin, the hurdle location can generally be estimated reliably, as observations constrain the decrease from large near-trench to low plate interior velocities, within uncertainty bounds (Fig. 3). The hurdle is located at distances from the trench varying between 400 and 1000 km, except for the section of subduction zone with weakly coupled megathrust in Northern Peru ($4\text{--}9^\circ\text{S}$). The hurdle location generally largely tracks the eastern margin of the Andean orogen. Only landward of the weakly locked megathrust of Northern Peru, the trench-perpendicular gradient in the velocity component is low and the hurdle location is identified at distances beyond 1000 km from the trench, although the uncertainty on the location is very large and the nearest location within the confidence interval still tracks the eastern boundary of the orogen. The hurdle lies a few tens of km landward of the backthrust in southcentral Peru ($10\text{--}13^\circ\text{S}$). Further to the south, in Bolivia ($14\text{--}2^\circ\text{S}$), it follows the backthrust at the base of the mountain range. In northernmost Argentina there is no clear, active backthrust, but the hurdle traces the border of the Puna plateau. Immediately to the south, around 30°S , the hurdle is located in the middle of the Sierras Pampeanas.

For South America, the hurdle for trench-parallel velocities is located between 220 and 800 km from the trench, excluding the weakly coupled megathrust section. It is always closer to the trench

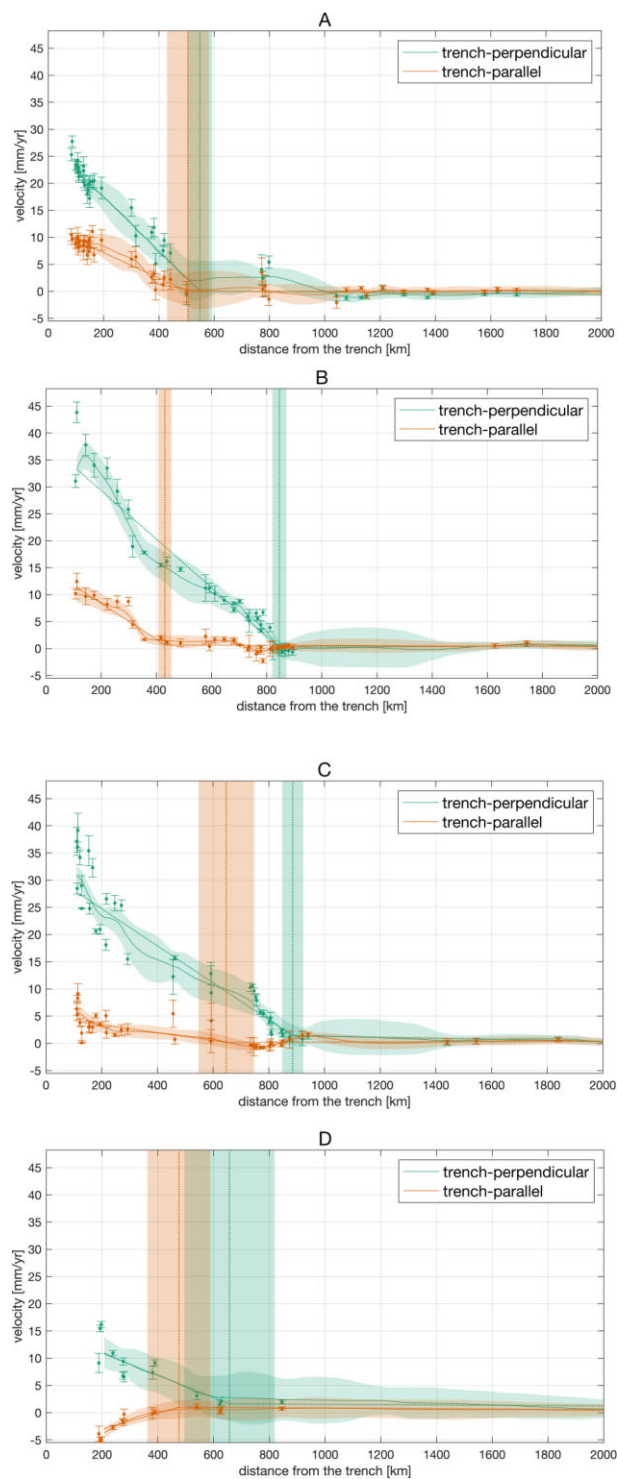


Figure 3. Continued.

or coincident with the trench-perpendicular hurdle within uncertainties. Velocities beyond the hurdle are near, but not always exactly, zero: the trench-perpendicular component is between -1 and 4 mm yr^{-1} in amplitude, while the trench-parallel component is between -1 and 2 mm yr^{-1} .

Observations of interseismic velocities in Sumatra are sparser than in South America. In the southeast of the island, both velocity components are small and have low gradients, including the near-trench region (Fig. 4). This reflects low megathrust coupling

in that region (Chlieh *et al.* 2008) and does not allow us to locate any hurdle. In central Sumatra, where near-trench velocities indicate strong interplate coupling and data coverage is much denser, we infer a hurdle in the trench-perpendicular component, bounding the zone of near-uniform low velocities in the interior of Sunda (Simons *et al.* 2007). The hurdle runs through the middle of the island, roughly coinciding with the southwestern edge of the Sibumasu terrane reported by Hutchison (2014) and Metcalfe (2011; Fig. 6b), as well as with the northeastern boundary of the zone of active orogenic deformation as indicated by Hall & Sevastjanova (2012). Trench-parallel velocities do not show a uniform decrease with distance from the trench, but rather are near-uniform on the Indian Ocean coast of central Sumatra and in the smaller offshore islands, and have a steep gradient over the Sumatran Fault (Prawirodirdjo *et al.* 1997; Genrich *et al.* 2000a), behind which the parallel velocities steeply decrease to zero. We thus do not estimate the hurdle location for trench-parallel velocities in Sumatra. In Java, both velocity components are low throughout, indicating low megathrust coupling (Koulali *et al.* 2017), and the lack of observations to the northeast of the island, in the Java Sea, prevents us from confidently identifying a hurdle.

Along the Japan trench, trench-perpendicular velocities decrease steeply with distance from the trench, with a constant or gently decreasing slope, in the vast majority of Hokkaido (trench locations north of 42°N) and most of central-northern Honshu (south of 40°N). The resulting hurdle location is $\sim 450\text{--}600 \text{ km}$ away from the trench (Fig. 5). It broadly follows the eastern margin of the Sea of Japan, a few tens of km offshore except for where it touches the northernmost tip of Hokkaido (Fig. 6c). On the other side of the Sea of Japan, observations in Manchuria and South Korea constrain the velocity field at intermediate to far distances, helping locate the hurdle. The trench-perpendicular and trench-parallel velocities in those sites are uniformly negative (around 5 mm yr^{-1} , both trenchward and right-lateral, respectively), indicating limited transpressional motion between Manchuria, inferred to be part of the Amurian Plate, and the Okhotsk Plate reference (Weaver *et al.* 2003; Petit & Fournier 2005). Off the northwestern shore of south-central Honshu (south of 40° latitude), observations in the intermediate- and far-field are not available and the velocity field is interpolated relying on observations far to the northwest and west, in Manchuria and South Korea. Nevertheless, the existence of a hurdle a short distance offshore in the Sea of Japan is supported by the steep, near-linear decrease with distance of trench-perpendicular velocities in Honshu and by the trench-perpendicular velocities on its northwestern coast being similar to those at the northwestern tip of Hokkaido and within less than 10 mm yr^{-1} of those in Manchuria. The Okhotsk–Amurian Plate boundary, inferred here to cross Honshu by Bird (2003), does not affect the slope of trench-perpendicular velocities with distance from the trench. In northernmost Honshu and the southwestern most tip of Hokkaido (for trench locations between 40° and 42°N), both the trench-perpendicular velocities and their trench-perpendicular gradients are lower, possibly reflecting lower interplate coupling than in laterally adjacent portions of the megathrust (Suwa *et al.* 2006; Hashimoto *et al.* 2009) or incomplete post-seismic transient corrections for the 1994 Sanriku earthquake (Loveless & Meade 2010).

Trench-parallel velocities in northern Honshu are low, while the uncertainties of available interseismic velocities are relatively high. This, combined with the narrow width where observations are possible, makes it difficult to identify a hurdle in the trench-parallel component. Additionally, trench-parallel velocities vary in sign across the study area. This clearly reflects in part small changes in the strike

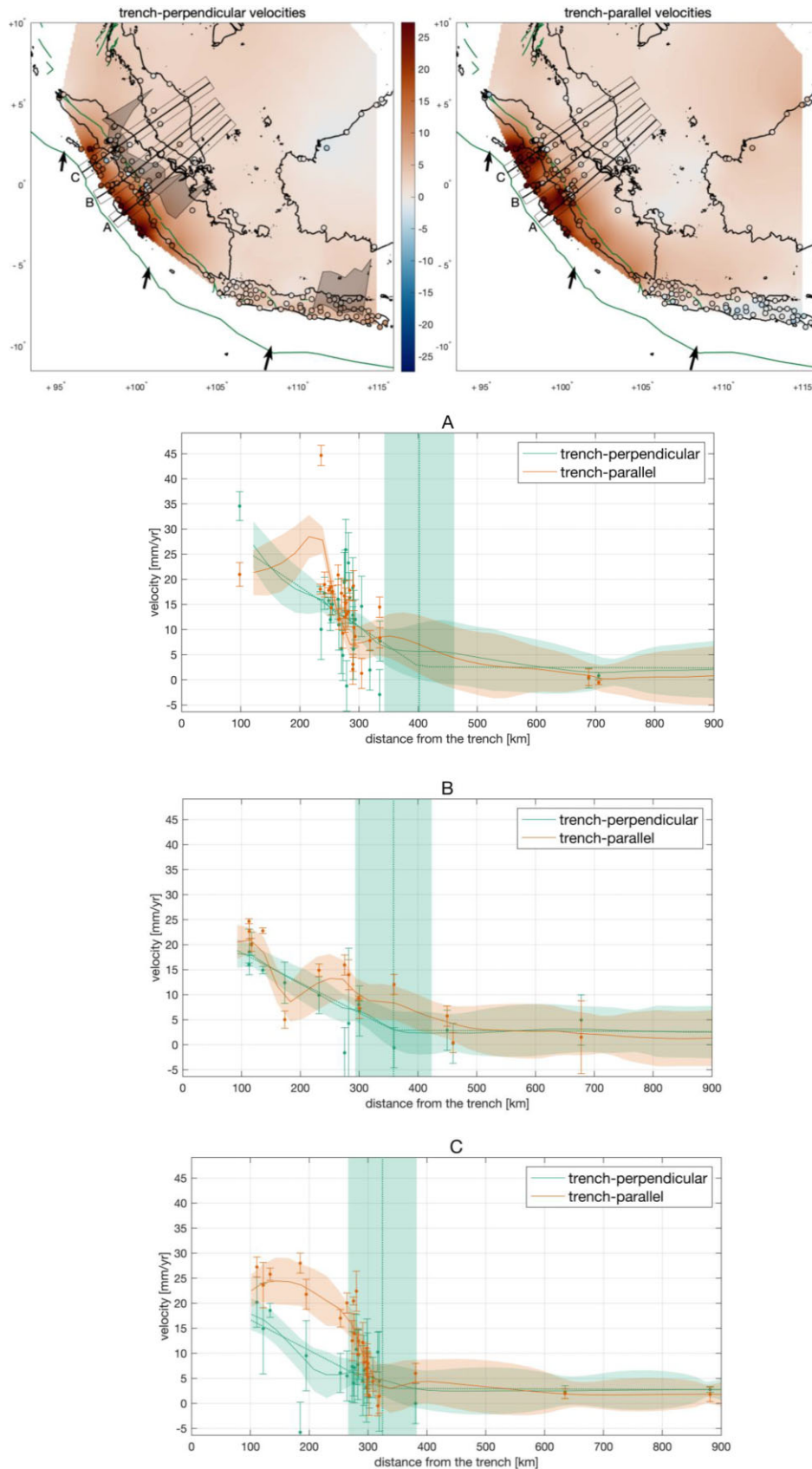


Figure 4. Estimated hurdle locations in southeast Asia. Please refer to caption of Fig. 3. Thick black arrows in the maps show interplate convergence between Sunda and Australian plates (Simons *et al.* 2007). The panels below the maps show trench-perpendicular and trench-parallel velocities, and hurdle locations along profiles (A–C) in Indonesia and Malaysia. Video S2 shows trench-perpendicular cross-sections along the entire margin.

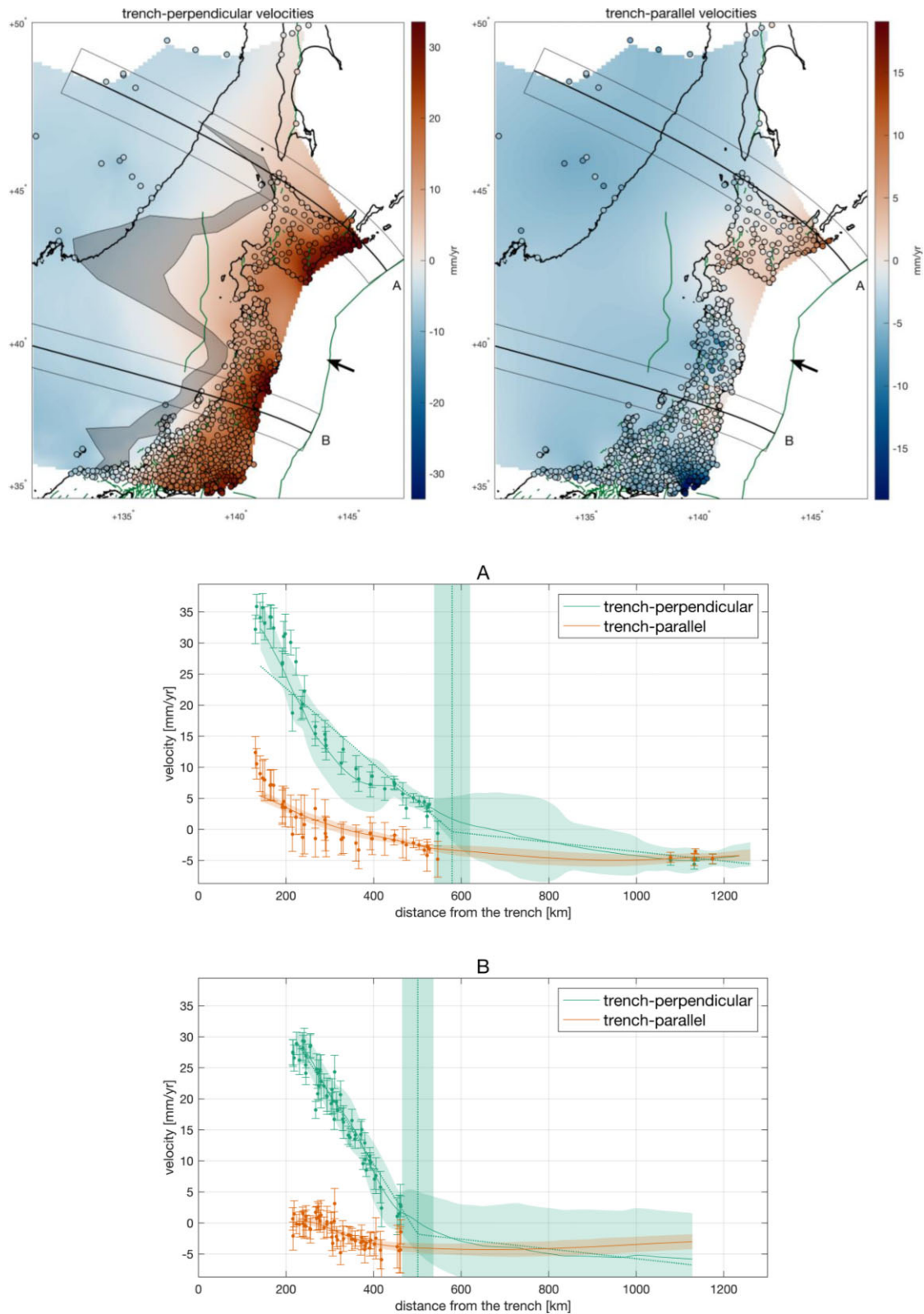


Figure 5. Estimated hurdle locations in Honshu and Hokkaido. Please refer to the caption of Fig. 3. Thick black arrows in the maps show interplate convergence between the Pacific Plate and Okhotsk (Kreemer *et al.* 2014). The panels below the maps show trench-perpendicular and trench-parallel velocities, and hurdle locations along profiles A (Hokkaido) and B (Honshu). Video S3 shows trench-perpendicular cross-sections along the entire margin.

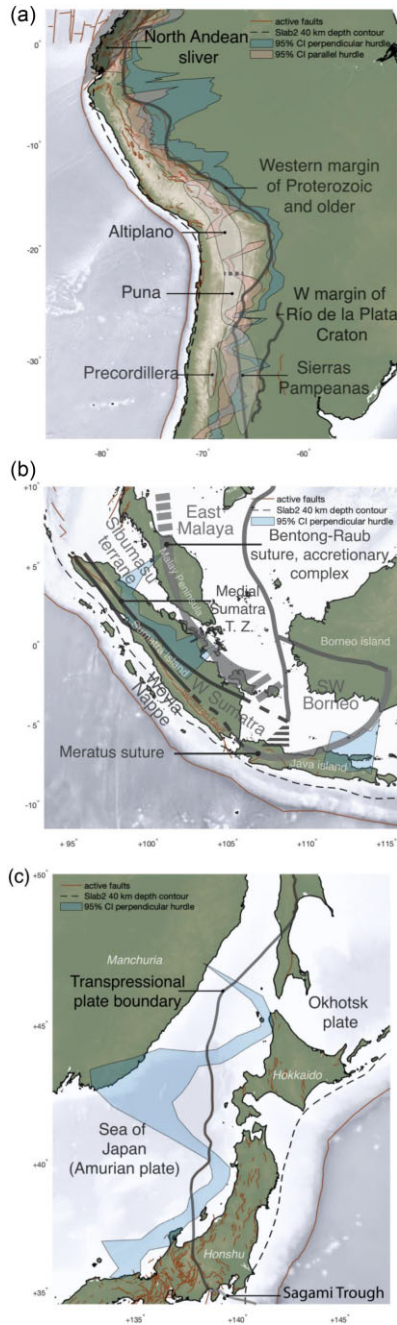


Figure 6. Comparison of hurdle locations with main geological features for our study regions. The panels show 1σ regions of hurdles for trench-perpendicular velocities in transparent blue regions, and for trench-parallel velocities in pink (cf. Figs 3–5). Active faults are shown red. The black dashed line shows the 40-km depth contour of the top of the slab (Hayes *et al.* 2018). The panels show major tectonic and geological features that are discussed in the text, where dashed lines indicate inferred or disputed locations. (a) For South America, the eastern front of the Precordillera, the broad location of the Sierras Pampeanas and the western edge of the Río de la Plata Craton are taken from Álvarez *et al.* (2012), while the orange line marks the approximate extent of the Proterozoic and older crustal domains (Chulick *et al.* 2013). (b) For Sunda, the location of the Meratus suture and Southwest Borneo crustal block is taken from Haberland *et al.* (2014) and Metcalfe (2011), while the Medial Sumatra Tectonic Zone and the crustal domains in Sumatra and the Malay peninsula are taken from Hutchison (2014) and Metcalfe (2011). (c) For Japan, plate boundaries are from Bird (2003).

of the trench which, combined with the overall head-on character of the convergence, changes the sign of the trench-parallel component of the velocity of the downgoing (Pacific) plate with respect to the overriding (Okhotsk) one. Interpolated trench-parallel velocities seem to decrease to uniform values (-5 to -6 mm yr^{-1}) within ~ 600 km of the trench in northern Hokkaido and within ~ 300 – 400 km in northern Honshu. However, precisely locating the hurdle is difficult because GNSS observations are only available onshore, in Japan and Manchuria, not in the Sea of Japan. Therefore, we do not perform our parallel hurdle location estimation in northern Japan.

We also performed the data analysis for Japan expressing all velocities with respect to the Amurian Plate, rather than the Okhotsk Plate, see Fig. S13. This results in an increase of all trench-perpendicular velocities by ~ 6 mm yr^{-1} , making them positive everywhere and reaching very close to 0 in Manchuria. However, the estimated trench-perpendicular hurdle location remains unchanged. Trench-parallel velocities increase uniformly also, by ~ 5 mm yr^{-1} . They thus become largely positive (dextral), except for a few isolated areas. Therefore, even though Manchuria is arguably on a different plate than Hokkaido and northern Honshu and it moves with respect to a stable Okhotsk reference, it seemingly behaves as the stable plate interior of the Japan Trench subduction zone. The estimated hurdle location is indifferent to whether the Okhotsk or Amurian Plate is used as a reference.

2.6 Discussion and conclusions of the data analysis

Trench-perpendicular velocities decrease with distance from the trench in a semi-linear fashion to low values, and both the velocities and the velocity gradient are distinctly lower beyond that. We refer to the region where the velocity gradient changes as a hurdle. The existence and location of the hurdle is supported by the fact that (1) the near-trench trend in velocities is derived from abundant observations, and that (2) observed velocities close to the hurdle are small and similar in value to observations much farther from the plate margin. The inferred hurdle differs therefore from the potentially detrimental effect that uneven spatial distribution of GNSS stations can have on interpolated strain rates and gradients in that it may result in spurious high-strain areas (e.g. Hackl *et al.* 2009). Our interpolation procedure is designed to give robust estimates of velocities including uncertainties that arise from both uneven spatial sampling and data uncertainties, and we propagate these uncertainties into our hurdle estimates.

The hurdle for trench-perpendicular velocities is located within 1000 km or less of the trench along the three studied subduction zones. Trench-parallel velocities sometimes have complex patterns, partly due to curvature of the margin. In South America, parallel velocities also decrease semi-linearly with distance from the trench up to a hurdle that either is located closer to the trench than the trench-perpendicular hurdle or, less commonly, roughly coincides with it. Hurdle locations broadly, but not precisely, follow the inland boundary of the orogen wherever such boundary is clearly expressed.

That the trend of trench-perpendicular velocities as function of distance deviates from a smooth decrease was first noted by Norabuena *et al.* (1998) for the northern portion of the Central Andes (the Altiplano of Peru and Bolivia) and Brooks *et al.* (2003) for the Southern Andes. The authors focus on the locally steep velocity gradient at the eastern edge of the Andes and explain the observations by active backarc convergence or sliver motion, which has

remained a popular explanation (Bevis *et al.* 2001; Brooks *et al.* 2003, 2011; Kendrick *et al.* 2006; Métois *et al.* 2013; Weiss *et al.* 2016; McFarland *et al.* 2017; Herman & Govers 2020; Shi *et al.* 2020). This explanation implies that interseismic strain accumulation involves non-recoverable strain on active backthrust faults or shear zones. The fold-and-thrust belt at the eastern margin of the Altiplano-Puna plateau, at roughly 11–22°S latitude, is bounded by a well-defined thrust front and is indeed considered to be actively deforming, despite little recent seismic activity (Brooks *et al.* 2011; Wimpenny *et al.* 2018). Farther north in Peru (4–11°S) and farther south in Argentina (around 31°S), earthquakes indicate that permanent strain occurs by thrusting in the eastern foreland of the Andes (Jordan *et al.* 1983; Sébrier *et al.* 1988; Alvarado & Ramos 2011; Rivas *et al.* 2019). However, active and continuous backthrusts faults appear to be absent in some locations, specifically at 22–29°S and south of 32°S latitude in South America, throughout Sumatra and Java and south of 39°N and north of 45°N off the west coast of Japan. Elsewhere, in the Sea of Japan, the inferred active faults marking the Okhotsk–Amur Plate boundary do not coincide with the location of the hurdle (Figs 2–5).

Even where active backthrusts have been observed, their role in explaining the spatial distribution of surface velocities may have been overestimated because of unrealistic model assumptions. Most studies that model the effect of backarc convergence on interseismic velocities assume a fully elastic Earth during the entire earthquake cycle. This is a particularly unrealistic assumption during the late interseismic period, when the mantle wedge is effectively fluid and it strongly underestimates far-field horizontal velocities and therefore may lead to incorrect interpretations of the observations (Trubienko *et al.* 2013; Li *et al.* 2015). Shi *et al.* (2020) do use a more realistic viscoelastic rheology to arrive at the conclusion that the backthrust is the cause of velocity distribution. However, they assume a hard backstop on their model overriding plate at a distance only ~150 km from the backarc thrust front. The decrease in trench-perpendicular velocities with distance from the trench is less linear than observed in their model, while the backthrust included in their model produces only local velocity offsets at the backthrust. Other modelling studies invoking backarc convergence require basal detachment faults extending in the trench-normal direction for ~200 km or more (Brooks *et al.* 2011; Weiss *et al.* 2016; McFarland *et al.* 2017). This may be unrealistic, considering that the E–W extent of the currently active central Andean backarc fold-and-thrust belt is only ~70 km wide (Pearson *et al.* 2013). Other authors treat the contact between the Andean orogen and the South American interior as a plate boundary, implying that it cuts through the entire lithosphere, slipping freely at depth, and that it is laterally continuous all along the orogen. Because of the extreme spatial extent and continuity of the modelled thrusts or plate boundaries, these studies probably overestimate the geodetic imprint of the localized shortening at the eastern edge of the Andes. Additionally, seen at the continental scale, the sharp, localized velocity decrease that has been used as evidence for backthrust slip (Norabuena *et al.* 1998; Brooks *et al.* 2011; Weiss *et al.* 2016; Shi *et al.* 2020), constitutes a relatively minor deviation from a general trend of steep but gradual decrease over the whole orogen (Fig. 3, profiles B and C). Furthermore, the aforementioned studies investigating the spatial distribution of interseismic velocities do not consider whether significant far-field coseismic displacements can be explained by their models. Within the framework of the earthquake cycle, we think there should be consistency in terms of coseismic slip and slip deficit accumulation, response of fault slip and creep to the stress evolution during the cycle, and boundary conditions.

Active faults are the possible cause of hurdle behaviour in some regions. North of ~3°S in South America, in southern Ecuador and Colombia, convergence is highly oblique and subparallel to a system of strike-slip and thrust faults (Veloza *et al.* 2012) that roughly coincides with the location of the hurdle in both velocity components. Localization of interseismic velocities might be chiefly caused by the fault system, consistently with the interpretation of this fault system as bounding a distinct, internally deforming North Andean sliver (e.g. Kellogg *et al.* 1995; White *et al.* 2003; Nocquet *et al.* 2014; Alvarado *et al.* 2016). Indeed, trench-parallel velocities at ~2°S are roughly constant within ~200 km from the trench and very steeply decrease at the location of the located hurdle and of major active faults, to lower, uniform values in the plate interior, consistently with the hypothesis of a distinct crustal sliver adjacent to the trench (cross-sections 200 and 201, Video S1). However, farther north both interpolated velocities components again decrease steeply and roughly uniformly with distance, with no evidence of an internally rigid sliver. In Sumatra, instead, trench-parallel velocities seem to be governed by the active strike-slip Sumatra Fault (Prawirodirdjo *et al.* 1997; Genrich *et al.* 2000a), well visible in cross-sections 34–41 of Video S2. Trench-parallel velocities also suggest strike-slip motion between southern Hokkaido (on the Okhotsk Plate per Bird 2003) and northern Manchuria (on the Amurian Plate), but the lack of GNSS observations in the Sea of Japan precludes a specific localization of the boundary from a purely geodetic perspective.

Trench-perpendicular velocities in all three study areas show a consistent steep decrease with distance from the trench. Trench-parallel velocities in South America show a similar trend almost everywhere, except for the southern end of the hypothesized North Andean sliver at ~2°S, the transition in obliqueness of the subduction relative to the local trend of the trench around ~20°S, and a small region of uniform near-trench velocities within 200 km of the trench at ~23°S that might reflect intra-Andean strike slip motion (Video S1). This suggests a more universal cause of the observed hurdles than fault zones. We find no correlation between the average dip of the shallow portion of the megathrust and hurdle location, since the former, represented by the horizontal distance between the trench and the 40 km megathrust depth contour, changes very little along the studied trenches (Fig. 6). We therefore focus on a possible explanation involving the overriding plate. Although the thrust faults in the Andean backarc are unlikely to directly account for the decrease in observed velocities as we move away from the trench, they are likely associated with a mechanical contrast between the deformed and partly accreted Andean region and the interior of the South America Plate. We thus hypothesize that such a contrast exists in this and other subduction zones, that it is responsible for the behaviour of interseismic velocities, and that a uniform overriding plate cannot account for observations.

The effective elastic thickness T_e derived from flexure observations is much lower at the margin than in the interior of South America (Stewart & Watts 1997; Pérez-Gussinyé *et al.* 2007, 2008). Variations in effective elastic thickness may derive from variations in thickness, composition, temperature, rheology and on the age of the load (Watts 1981; Burov & Diament 1995). The effective elastic thickness is derived from lithospheric flexure on geological timescales and is not directly applicable to the predominantly horizontal plate loading over interseismic timescales. It is very likely however that a relevant mechanical contrast exists. The load-bearing capacity of the low-viscosity mantle wedge is negligible on (interseismic) timescales, meaning that the contrast is most likely related to properties of the overriding plate. The bulk of the interseismic shortening of the overriding plate is recovered during megathrust

earthquakes, so it can be considered largely elastic. A mechanical contrast that is relevant in the context of earthquake cycles is thus a compliance contrast or thickness contrast. Below we present mechanical models aimed at exploring our hypothesis that (interseismic) hurdles are a consequence of such contrast, whilst also showing significant coseismic displacements beyond the hurdle.

The presence of stiff cratonic lithosphere in the interior of the South American Plate in central Argentina was proposed as the explanation for the relatively low horizontal post-seismic velocities in the region (compared to model results without such a craton) by Klein *et al.* (2016). Itoh *et al.* (2019), instead showed that a compliant arc and backarc region can explain the high gradient of onshore horizontal interseismic velocities with distance from the trench in Hokkaido. We hypothesize that a mechanical contrast between more compliant lithosphere at the convergent margin of the overriding plate (in the arc and backarc region) and less compliant lithosphere of the interior of the plate can explain the observed near-trench localization of high spatial gradients of horizontal surface velocities. We thus propose that such a contrast, while avoiding artificially fixed model edges in the vicinity of the trench, can produce a hurdle in interseismic velocities and surface motion generally consistent with observations throughout the seismic cycle, even though we specifically focus here on interseismic observations.

3 NUMERICAL MODEL

3.1 General concept

To study the interseismic and coseismic surface deformation field we develop a 3-D mechanical model. We seek to explain observation trends at different margins, that is the semi-linear decrease of interseismic velocities from the trench to the hurdle, the low interseismic strain accumulation beyond it, but significant far-field coseismic displacements due to a megathrust earthquake. We test whether these trends may be a consequence of a compliancy contrast in the overriding plate. In the context of our model, we use a contrast in Young's modulus E and shear modulus G , with the same ratio between the two moduli, in an overriding plate with a uniform thickness and Poisson's ratio ν . Rather than representing realistic averages of the elastic properties of the lithosphere, the model Young's modulus values proxy for a more general ability of the plate to resist intraplate stresses resulting from the total thickness, composition and thermal state of the real lithosphere. The modelled contrast in the elastic properties of the overriding plate consists of a relatively low Young's modulus in the 'near-trench' region and a higher modulus in the far-field. The assumed geometry of the slab and overriding plate in the model is not specific for any margin and instead follows a realistic trench-perpendicular slab profile (Fig. 7). We consequently do not expect to reproduce specific regional observations with the model.

Model deformation is driven by slab motion and periodic unlocking of asperities. The slab itself is kinematically driven, as up dip and down dip end of the slab are driven at the interplate convergence rate. Coseismic slip and afterslip are not imposed kinematically and are instead physically determined, together with viscous relaxation, by the asperity size and location and by the mechanical properties of the material in the model. Govers *et al.* (2018) show that coseismic slip increases per earthquake cycle until no variation occurs from one cycle to the next and physically consistent pre-stresses have developed.

3.2 Model domain and rheology

We have chosen the model domain size so that boundaries and boundary conditions do not affect the results in our region of interest; the trench-perpendicular (x) model extent is 2200 km, 2000 km in the trench-parallel direction (y) direction, and 338 km in the depth (z) direction. The trench is located at $x = 0$, while the oceanward model boundary is located at $x = -212$ km. The surface downgoing plate has its upper surface at a depth of 8 km, and the overriding plate at $z = 0$. The subducting plate has a thickness of 80 km, consistent with the seismologically detected depth of the lithosphere–asthenosphere boundary of various oceanic plates (Kawakatsu *et al.* 2009; Kumar & Kawakatsu 2011). The overriding plate has a uniform 40 km thickness, except at the taper due to the megathrust geometry at the bottom and at the slope down to the trench over 18 km horizontal distance.

The model slab and the overriding plate are elastic, and the mantle wedge and slab asthenosphere are viscoelastic with a Maxwell rheology. We model seismic cycles with quasi-dynamic slip on discrete faults and shear zones (see Section 3.4 and Govers *et al.* 2018; Section 2). After model spin-up, the model has identical megathrust earthquake cycles with a return period of 300 yr. Post-seismic relaxation in the model involves the two most relevant large-scale processes, afterslip and viscous relaxation (Bürgmann & Dresen 2008; Diao *et al.* 2014; Broerse *et al.* 2015; Klein *et al.* 2016). Our reference model has a mantle viscosity η of 10^{19} Pa·s. Throughout the model domain, outside of the overriding plate, the elastic moduli are uniform: Poisson's ratio ν is 0.25 and Young's modulus E is 100 GPa, consistently with values from PREM (Dziewonski & Anderson 1981) in the 0–40 km depth range. In particular, the ν value of 0.25 consists of the common Poisson solid assumption (e.g. Melosh & Raefsky 1983) and is very consistent with the values determined for lower crustal and mantle lithologies, while being at the lower end of the realistic range for the upper crust. The return period thus is ~ 37.9 characteristic relaxation (Maxwell) times long, so that about 55 per cent of the model cycle period is interseismic, given that the earthquakes on the different asperities within one cycle occur within 40 yr of each other (Govers *et al.* 2018).

3.3 Numerical method

We use a finite element method to solve the time-dependent 3-D mechanical equilibrium equations for given material properties and boundary conditions including a free surface, as detailed below. Finite element platform *GTECTON* version 2021.0 uses the Portable, Extensible, Toolkit for Scientific Computation (*PETSc* version 3.10.4; Balay *et al.* 1997, 2021a,b) and *OpenMPI* (version 3.0.0; Gabriel *et al.* 2004) to solve the time-dependent mechanical problem in parallel (e.g. Govers & Wortel 2005; Govers *et al.* 2018).

Each model includes 384 566 nodes arranged in 2238 109 tetrahedral elements and 1284 193 total degrees of freedom. These choices are based on pilot models to find a mesh where surface deformation is insensitive to further grid refinement. A posteriori estimates of the model error (Verfürth 1994) for the selected mesh are small enough to support our conclusion that our results are accurate within a few per cent.

3.4 Modelling the megathrust

Dynamic differential slip on the megathrust is modelled using the slippery nodes technique (Melosh & Williams 1989). Five asperities on the otherwise freely slipping megathrust are fully coupled

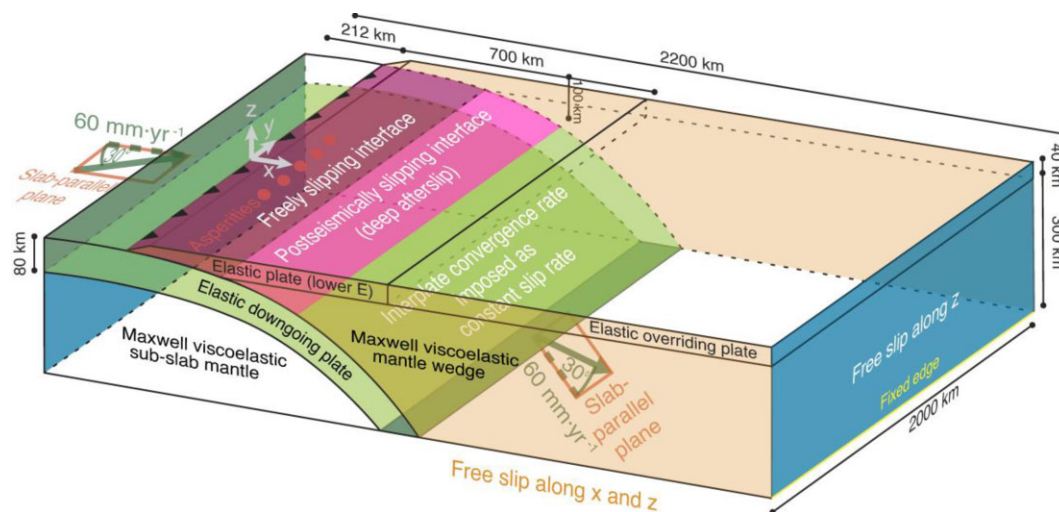


Figure 7. Schematic representation of the finite element model domain with its geometry, spatial extent, coordinate system, main mechanical properties and the applied boundary conditions.

(locked) during all stages of the earthquake cycle, except during the coseismic phase when unlocked asperities can slip freely. Treating the megathrust away from the asperities as freely sliding is consistent with observations of megathrust regions immediately up- and downdip of the asperities sliding stably and with low friction (Scholz 1998; Ikari *et al.* 2011; Hardebeck 2015).

The asperities are circular in map view and have a diameter of 50 km, consistent with the inversion results of Herman & Govers (2020). They are centred at a horizontal distance of 120 km from the trench and 100 km from each other, resulting in accumulation of slip deficit (locking and pseudo-locking) on and around the asperities, over an along-trench distance of ~ 500 km (Herman *et al.* 2018). At the start of each new 300-yr cycle, the middle asperity first has its coseismic phase. After a delay of 20 yr, the intermediate asperities have their coseismic phase. After 20 more years, the outer asperities have the coseismic phase. Each asperity has its coseismic phase every 300 yr. Every coseismic phase is instantaneous and consists of the relevant asperities being unlocked, the megathrust slipping freely and the asperities being relocked, all with no model time elapsing. All slip deficit accumulated on the megathrust interseismically due to each asperity is released during its coseismic phase. The distribution of coseismic slip is thus determined by the asperities and by the mechanical properties of the plates and asthenospheric mantle. Coseismic slip can occur at depths shallower than 40 km, as that is the maximum depth of the overriding plate and thus of the megathrust.

Coseismic slip, although traditionally thought to not extend to very shallow depth because of unconsolidated material in the hanging-wall (Kanamori 1972; Moore & Saffer 2001), can indeed propagate up to the trench (Fujiwara *et al.* 2011; Sladen & Trevisan 2018). We minorly restrict coseismic slip on the updip portion of the megathrust, above 15 km depth, by applying (small) shear tractions that are proportional to the coseismic fault slip amplitude, with a spring constant of 200 Pa m^{-1} .

Downdip of the megathrust, the contact between the subducting plate and the mantle wedge (depths >40 km in our models) is often viewed as a viscoelastic shear zone (Tichelaar & Ruff 1993; van Keken *et al.* 2002). In our model, we represent it as a discrete interface that slips freely interseismically and is fully locked coseismically. Additionally, immediately after each coseismic phase, we include an instantaneous afterslip phase, during which the shear

zone, together with the megathrust outside of the asperities, slips freely until mechanical equilibrium is reached. The shear zone thus resolves coseismic stress changes as much as possible via afterslip and creeps interseismically, but behaves as part of the mechanical continuum responding elastic to coseismic slip on the megathrust. This implementation has the significant benefit of avoiding the computationally demanding simulation of viscous flow in a narrow channel, while capturing the main features of interseismic and coseismic behaviour and while producing afterslip with no need to impose it kinematically. Govers *et al.* (2018) used a similar approach, and they defined ‘primary afterslip’ as immediate viscous slip on the shear zone in response to coseismic stress changes that is generally thought to occur much more quickly than bulk viscous relaxation in the mantle wedge (Govers *et al.* 2018; Muto *et al.* 2019). ‘Secondary’ afterslip also occurs on the deep shear zone, over time, in response to bulk viscous relaxation during the post-seismic phase.

Afterslip on the deep shear zone is commonly assumed to occur at depths shallower than about 80–100 km (Diao *et al.* 2014; Sun *et al.* 2014; Yamagiwa *et al.* 2015; Hu *et al.* 2016; Freed *et al.* 2017). Klein *et al.* (2016) showed that allowing relative motion between the mantle wedge and the slab, by introducing a narrow low-viscosity zone between 70 and 135 km depth along the top of the slab, produces little change in post-seismic horizontal surface motion. In our model, we therefore allow afterslip, and interseismic slip deficit accumulation, on the shear zone downdip of the megathrust only at depths smaller than 100 km.

We aim to capture deformation and flow of the mantle wedge and asthenosphere in response to stress changes during the earthquake cycle. To exclude modelling steady-state mantle flow on geological timescales that is irrelevant for the seismic cycle, we use the finite element split node technique (Melosh & Raefsky 1981) to impose the slab velocity beyond a depth of 100 km. Similarly, we avoid driving long term subslab asthenosphere by applying the slab velocity along the base of the slab. We remove a small residue of long-term deformation of the model related to stretching and unbending of the slab that we identify from an identical model without asperities or earthquakes. This approach facilitates loading of the mantle wedge and subslab asthenosphere by non-steady velocity–stress perturbations during all stages of the earthquake cycle, without neglecting the role of the viscoelastic rheology of either the oceanic or the continental mantle.

3.5 Boundary conditions

We impose the updip and downdip ends of the downgoing plate to move obliquely at the interplate velocity in the direction parallel to the slab surface. The trench-perpendicular component of the velocity is 60 mm yr^{-1} . Given the linear nature of the rheology used, the obliqueness angle of the interplate convergence simply linearly scales the magnitude of the trench-parallel velocities resulting from megathrust coupling, without affecting the trench-perpendicular velocities. An arbitrary angle of 30° (counter-clockwise) is chosen, measured from the trench-perpendicular direction in a slab-parallel plane, implying a trench-parallel component of the velocity of 34.64 mm yr^{-1} (Fig. 7). We verified that the presence and magnitude of the trench-parallel velocity does not affect trench-perpendicular late interseismic surface velocities or coseismic surface displacement. We apply a free-slip boundary to the remaining lateral, vertical sides of the model, while we allow only vertical motion at the landward end and fix the bottom landward and oceanward edges of the vertical sides.

Restoring pressures impose isostasy along the free surface of both plates (Govers & Wortel 1993). These pressures act perpendicularly to the surface and have a magnitude directly proportional to displacement in that direction. The constant of proportionality is the gravitational acceleration (9.8 m s^{-2}) times the density contrast— 3250 kg m^{-3} at the top of the overriding plate, 2200 kg m^{-3} at the top of the oceanic plate.

4 MODELLING RESULTS AND ANALYSIS

4.1 Reference model

In our reference model, the overriding plate has a Young's modulus of 50 GPa within 700 km horizontal distance from the trench and of 250 GPa beyond. Fig. 8 shows the resulting surface deformation. Figs 8(a) and (c) show interseismic velocities 260 yr after the last earthquake on any asperity, that is after ~ 33 Maxwell times and immediately before the next 40-yr earthquake sequence on the five asperities. Both the trench-perpendicular and trench-parallel velocity components decrease with distance from the locked asperities. The transect through the central asperity in Fig. 8(c) (solid line) shows a roughly linear decrease in the trench-perpendicular velocity with distance from the trench, from the peak value (above the asperity) to the location of the contrast, where the gradient decreases sharply. Here, the trench-perpendicular velocity is ~ 10 per cent of the interplate convergence rate and ~ 8 per cent of the peak value. Beyond the contrast, the trench-perpendicular velocity in the far-field decreases gradually to zero at the far end of the model, which is a consequence of the model boundary condition there. Trench-parallel velocities along this transect instead decay with a progressively shallower slope away from the peak (Fig. 8c). They reach a near-zero value at the compliance contrast and reach ~ 10 per cent of the peak value ~ 200 km closer to the trench. The steeper decrease in the trench-parallel component causes velocity directions in the locked portion of the subduction zone to rotate from convergence-parallel to trench-perpendicular with distance from the trench (Fig. 8a). The results thus show slow and mostly trench-perpendicular interseismic strain accumulation beyond the contrast. The mechanical contrast thus results in hurdle-type behaviour comparable to what we infer from the GNSS data. The hurdle is expressed in both horizontal velocity components, albeit more clearly in the trench-perpendicular velocities.

Interseismic velocities 500 km to the north of the middle of the model (Figs 8a and c) are substantially slower than above the central asperity. They are higher than velocities 500 km to the south of the central asperity, showing that oblique convergence results in a distinctly asymmetric pattern of interseismic strain accumulation. Particularly the trench-parallel velocity differs. Trench-parallel velocities along the northern transect in Figs 8(a) and (c) increase with distance from the trench before decreasing again. Fig. 8(a) shows that, in a trench-perpendicular profile 500 km the south of the middle of the model, trench-parallel velocities decrease with distance from the trench. Trench-perpendicular velocities on both lateral sides decrease with distance from the trench. The imprint of the contrast on the (gradient of the) velocities is less pronounced away from locked asperities than in the central region.

Unlocking of the central model asperity results in coseismic slip on the megathrust. The coseismic slip on the megathrust corresponds to a moment magnitude $M_w = 8.7$, computed using the average elastic shear modulus of the overriding and subducting plates. Fig. 8(b) shows coseismic horizontal surface displacements in the overriding plate. The displacement magnitude is highest (~ 11 m) and obliquely ocean directed above the ruptured asperity. Fig. 8(d) shows a steep decrease of trench-perpendicular displacement with distance from the trench, and a change in the gradient at the mechanical contrast. Trench-parallel displacements are less affected by the contrast. However, both components are significantly non-zero beyond the compliance contrast.

4.2 Lateral compliance contrast versus a homogeneous plate

We compare the results of our reference model with results from two other models, both with an overriding plate with a uniform Young's modulus, and all else the same as in the reference model (Fig. 8c). We find that a uniform value of 10 GPa produces a steep decrease in both interseismic velocity components, that is it concentrates interseismic strain closer to the trench. However, it lacks significant trench-perpendicular coseismic displacement in the far-field, with amplitudes below 10 mm at distances from the trench greater than 800 km, unlike our reference model. Furthermore, 10 GPa is a very low value for the Young's modulus of the whole lithosphere in the far-field as well as near-field. Conversely, a uniform, realistic value of 100 GPa for the overriding plate produces large far-field coseismic displacement. However, its trench-perpendicular interseismic velocities decrease slowly and have significant amplitudes (more than a third of the peak value) at the location of the contrast in the reference model (700 km from the trench).

We conclude that a uniform overriding plate cannot simultaneously explain the observed interseismic hurdle and far-field coseismic displacements. A compliance contrast in the overriding plate does explain an interseismic hurdle and far-field coseismic displacements.

4.3 Radial elasticity variations

Pollitz *et al.* 2011a, b) concluded that radial elasticity layering is needed for fitting both the near- and far-field coseismic static GNSS displacements following the Maule and Tohoku earthquakes. We evaluate to what extent a radial elasticity variation affects the model results. We use elastic moduli varying with depth according to PREM (Dziewonski & Anderson 1981; Pollitz *et al.* 2011a, b). The modelled interseismic surface velocities differ little from a model

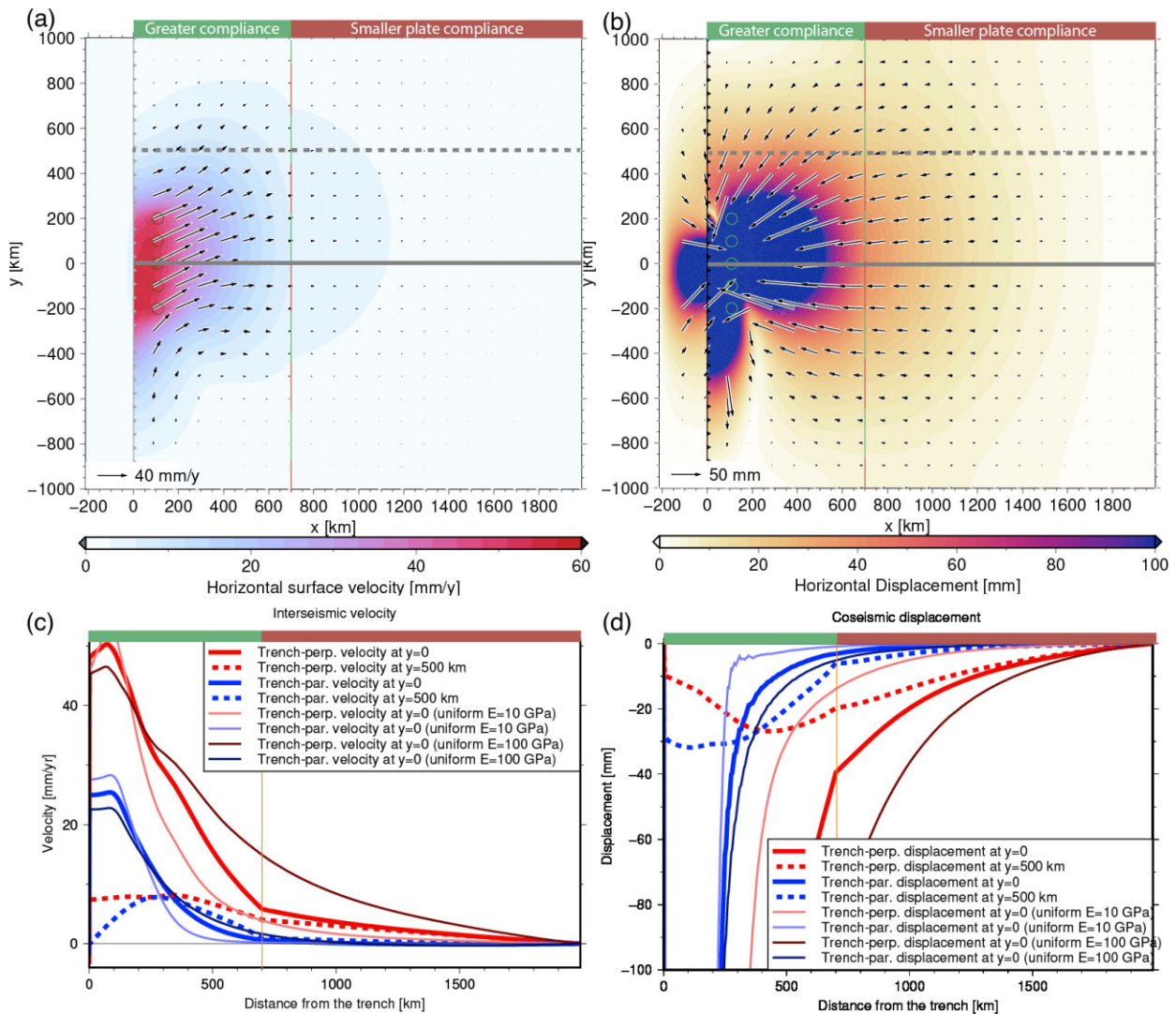


Figure 8. Reference model surface deformation and profiles. The extent of the forearc and backarc region with low Young's modulus E , and of the far-field region with high Young's modulus is shown above the panels. (a) Interseismic horizontal velocities at the end of the earthquake supercycle, immediately before the next unlocking of the central asperity. Colours show magnitudes, and vectors show directions and magnitudes. The black barbed line indicates the model trench that separates the subducting plate (left-hand panel) from the overriding plate (right-hand panel). Black circles are surface projections of locked asperities. Solid and dashed thick grey lines correspond with transect locations in panels (c) and (d). (b) Coseismic horizontal displacements due to unlocking of the central asperity. Colours show magnitudes, and vectors show directions and magnitudes of horizontal surface displacements. (c) Interseismic surface velocity components along transects on the overriding plate shown in (a) with the same line stroke (continuous or dashed). Positive velocities are landward, to the right. (d) Coseismic displacement components along a trench-perpendicular transects show in (b). Seaward displacement is negative, to the left.

with uniform Young's modulus $E = 100$ GPa (Fig. S15), being less than 5 per cent higher or lower and near-indistinguishable beyond 300 km of distance from the trench. We conclude that the hurdle-type response of interseismic velocities cannot be explained by the radial elasticity layering only. In the context of our numerical models a lateral contrast is thus needed in the overriding plate to reproduce the hurdle-like observations. In Sections 5.2 and 5.3, we address the tectonic and rheological viability of a mechanical contrast in overriding plates.

4.4 Importance of near-trench elasticity and of its contrast with far-field elasticity

The reference model uses a Young's modulus $E = 50$ GPa in the near-trench and $E = 250$ GPa in the far-field of the overriding

plate. The latter value is beyond the upper limit of ~ 200 GPa for lithospheric rocks (specifically eclogite; Christensen 1996; Aoki & Takahashi 2004). Here we explore the sensitivity of our model results to elastic properties.

We systematically vary the Young's modulus in both the near-trench and the far-field portion of the overriding plate. Figs 9(a) and (b) shows trench-perpendicular profiles of interseismic velocities through the central asperity for models where the Young's modulus is higher in the far-field than near the trench by a factor of 3 (red) and 5 (purple), with different average values (less continuous line strokes for lower values). We also vary the Young's modulus of the far-field while keeping the near-trench value the same (Figs 9c and d), the latter with a value of 50 GPa (purple), 30 GPa (dark red) or 20 GPa (orange) with less continuous line strokes for lower far-field values. In Figs 9(e) and (f) we do the

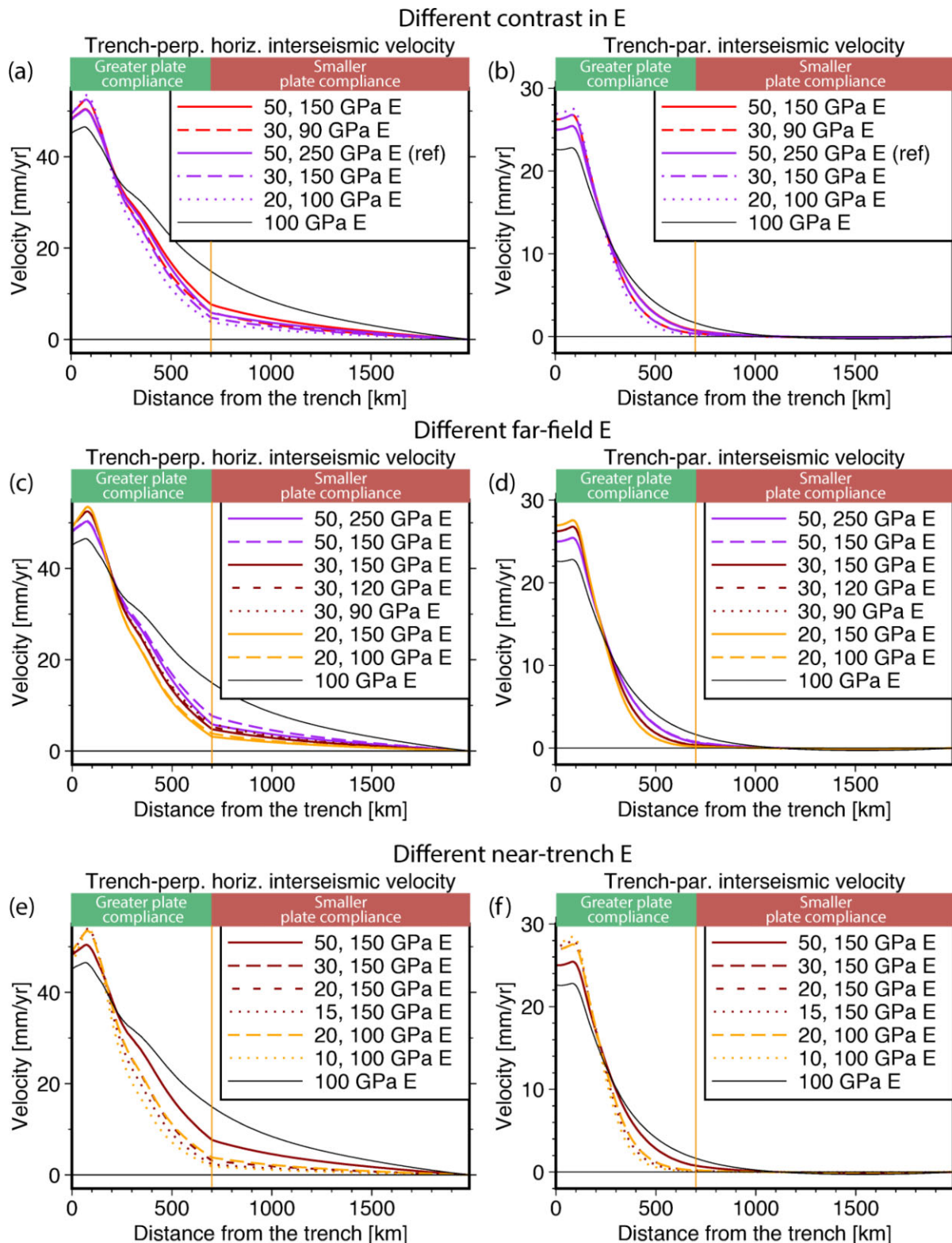


Figure 9. Sensitivity of interseismic velocities to a compliance contrast within the overriding plate. Panels show trench-perpendicular and trench-parallel components of interseismic velocities as function of distance from the trench along a transect through the central asperity (solid grey line in Fig. 7a). The extent of the forearc and backarc region with low Young's modulus E , and of the far-field region with higher Young's modulus is shown above the panels. The location of the contrast in E , if any, is also marked by the dark orange vertical line. (a, c, d) Trench-perpendicular velocity, and (b, e, f) and trench-parallel velocity. (a, b) Different average E values (different line strokes, less continuous for lower values) with the same contrast (ratio) between near-trench E and far-field E (same colour). (c, d) Different far-field E values (different line strokes, less continuous for lower values) with the same near-trench E values (same colour). (e, f) Different near-trench E values (different line strokes, less continuous for lower values) with the same far-field E values (same colour). The model with a uniform of E of 100 GPa is always shown in black.

opposite, showing the effect of different values of Young's modulus in the near field (less continuous strokes for lower values) while keeping a far-field value of 150 GPa (dark red) or 100 GPa (orange).

Looking at the trench-perpendicular velocities (Figs 9a, c and e), the results show that a larger contrast in E result in lower velocity amplitudes trenchward of the contrasts and steeper slopes in velocity, particularly between 200 and 300 km of distance from the trench, and in shallower slopes beyond the contrast (Fig. 9a). Lowering both values of E accordingly, while keeping the amplitude of the contrast unaltered, has a similar effect (Fig. 9a, different line strokes with the same colour). The effect of increasing the far-field value of E while keeping the near-trench value constant (Fig. 9c) is generally smaller than doing the opposite (Fig. 9e), but it is still noticeable when the near-trench E is high (Fig. 9c, purple lines). With lower near-trench E values, increasing the far-field E is hardly noticeable (Fig. 9c, dark red lines and orange lines). There is no sharp cut-off beyond which hurdle behaviour is exhibited, and a break in the slope of the profile is always present at the location of the contrast, if any. We take the trench-perpendicular hurdle to be a good indicator of the location of a compliance contrast in the overriding plate.

The amplitude (i.e. ratio) of the contrast in Young's modulus on trench-parallel velocities (Fig. 9b) is variable. This is because the far-field Young's modulus by itself has very little effect on the profiles of trench-parallel velocities (Fig. 9d). The near-trench Young's modulus alone controls the decrease in trench-parallel interseismic velocities with distance from the trench, with lower values causing a steeper decrease on the landward side of the peak velocity (Fig. 9f). We observe however that all curves (including the uniform E model) decrease to low velocities at the contrast, that is hurdle behaviour of trench-parallel interseismic velocities is not a very strong indicator for a compliance contrast.

Fig. 10 shows profiles of trench-perpendicular coseismic displacement (corresponding to an earthquake with $M_w = 8.7$) of the same models as in Fig. 9. The amplitude of the far-field displacement is controlled by the Young's modulus in the near-trench, more compliant portion of the plate, regardless of the contrast with the higher Young's modulus in the less compliant internal portion. Pollitz *et al.* (2011a) observed trench-perpendicular coseismic displacements after the $M_w = 8.8$ Maule earthquake up to a few tens of millimeters beyond 700 km from the trench. A near-trench Young's modulus $E \geq 20$ GPa is needed for a coseismic displacement greater than 20 mm 700 km from the trench (where the contrast is located in the reference model), while a modulus of 50 GPa is needed for a displacement of 20 mm 1000 km from the trench. This need for a moderate E in the near-trench region, combined with the need for a sufficient E contrast to reproduce the hurdle behaviour in trench-perpendicular interseismic velocities, requires the use of a very high far-field E in the overriding plate of the reference model (Section 4.1) to produce realistic behaviour both interseismically and coseismically. If the far-field E is only moderately high (~ 100 GPa or less, for instance), the contrast between far-field and relatively near-trench E is probably insufficient to explain hurdle behaviour, given that coseismic displacement requires near-trench E to be moderate. In this case, the compliance contrast within the overriding plate, responsible for the hurdle, should be greater than implied by the elastic moduli of the constituent materials alone. In Section 5.3 we discuss the rheological implications of the model sensitivities presented here.

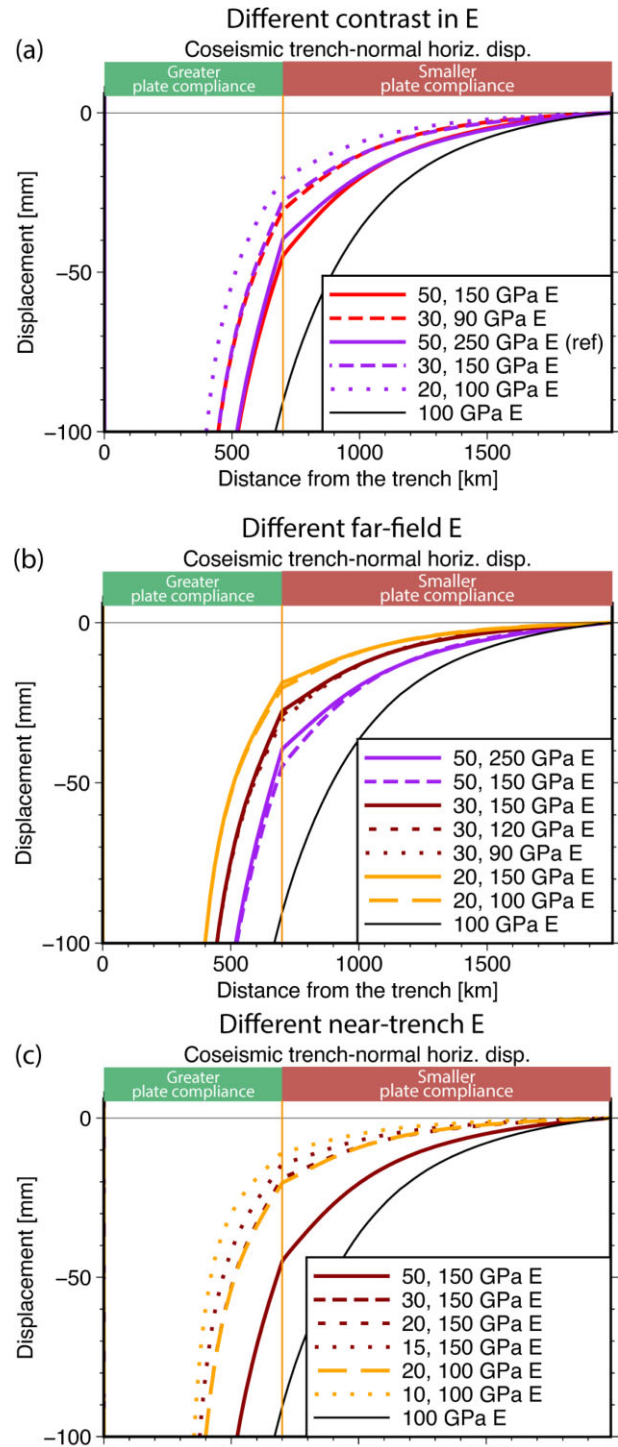


Figure 10. Sensitivity of coseismic displacements to a compliancy contrast within the overriding plate. Trench-perpendicular profiles of intermediate- and far-field trench-perpendicular coseismic displacement at $y = 0$, for models with different contrasts in E and for a uniform model as comparison. (a, b) Different average E values (different line strokes, less continuous for lower values) with the same contrast (ratio) between near-trench E and far-field E (same colour). (c, d) Different far-field E values (different line strokes, less continuous for lower values) with the same near-trench E values (same colour). (e, f) Different near-trench E values (different line strokes, less continuous for lower values) with the same far-field E values (same colour). The model with a uniform E of 100 GPa is always shown in black.

4.5 Shear modulus contrast in the overriding plate

We thus far focused on contrasts in Young's modulus E , which is the resistance to interseismic (elastic) shortening of the overriding plate in response to the head-on component of the convergence velocity. The resistance to (elastic) shear deformation due to the trench-parallel component of the convergence velocity is better represented by the shear modulus $G = \frac{E}{2(1+\nu)}$.

All presented models used a uniform Poisson's ratio $\nu = 0.25$, meaning that the contrasts in Young's modulus E and shear modulus G are the same. We now test whether varying the contrast in G while keeping the contrast in E constant, affects trench-perpendicular and -parallel velocities. The near-field and far-field values of E are 30 and 150 GPa, respectively, while ν is 0.2. We decrease the near-field G by 14 per cent through a drastic increase (doubling) in Poisson's ratio, to 0.4, which results in a slight change in the trench-parallel velocity, but does not alter the trench-perpendicular velocity (Fig. S16). Different contrasts in E and G are thus unlikely to affect the apparent hurdle location, particularly as determined in the trench-perpendicular component of velocities, justifying our use of the same contrast in both moduli.

4.6 Role of the location of the mechanical contrast

We investigate the sensitivity of the models to the location of the contrast in E by stepwise reducing its distance from the trench to 400 km in 100 km intervals. We do so in a model with a contrast that produces the largest differences in interseismic velocities compared to a uniform E (10 and 100 GPa; Fig. 9). Bringing the contrast closer to the trench most noticeably affects trench-perpendicular velocity profiles (Fig. 11a). Increasing the contrast distance produces less uniform decay of such velocities on the trenchward side of the contrast, as the slope becomes shallower before reaching the contrast. Instead, when the contrast distance is increased, the velocities at the contrast become lower while beyond the contrast, the slopes become flatter. Trench-parallel velocities are much less affected by the location of the contrast (Fig. 11b), as the near-trench value of E controls the general shape of the decrease. The presence of a single contrast in E can thus produce a varying distance between the apparent location of the hurdle (a sharp transition between a steep decay and near-0 amplitudes) in the two components of horizontal interseismic velocities, depending on the near-trench value of E and its spatial extent. Overall, the two horizontal velocity components not only have different spatial distribution with the same contrast, but also respond differently to variations in distance to the contrast or in the value of E on either side of the contrast. This behaviour is compatible with our observations showing that the apparent location of the trench-parallel hurdle relative to the trench-perpendicular one varies along a subduction zone and between subduction zones, rather than coinciding with it or being offset by a constant distance.

Interseismic locking results in steadily increasing shear tractions on asperities. The slope of the velocity curves in Fig. 11 represents horizontal strain accumulation rates in the overriding plate. In the region within 200 km from the trench, strain accumulation rates show to be insensitive to the distance of the contrast, and shear tractions on asperities are consequently expected to be insensitive to the width of the zone where strain accumulates. Fig. S15 shows indeed that the average traction on the middle asperity in the downdip direction increases little with decreasing trench-contrast distance; for instance, the traction becomes only ~ 3 per cent larger when the distance to the contrast reduces from 700 to 500 km. The temporal rate of change of this traction at the end of the cycle in the late

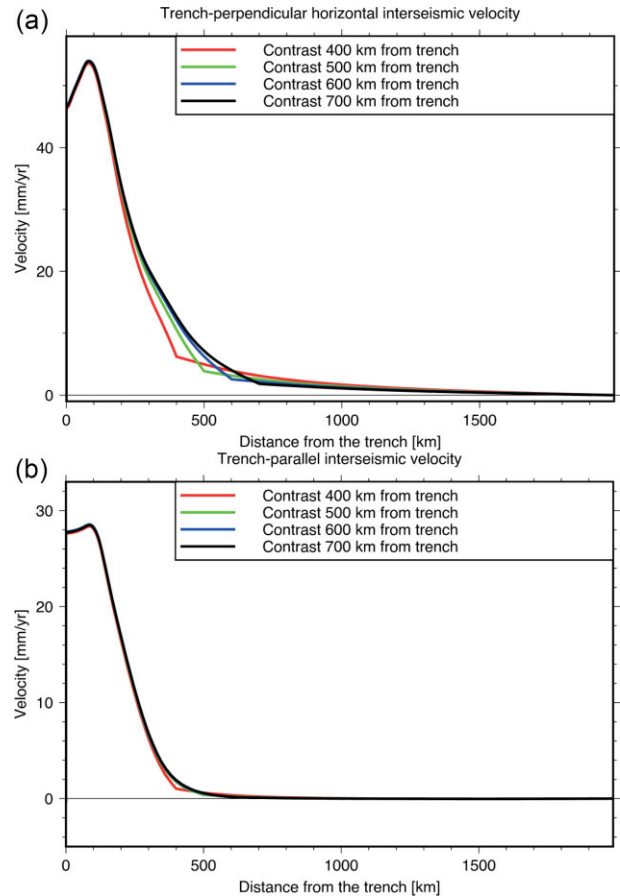


Figure 11. Sensitivity of interseismic velocities to the location of a compliancy contrast within the overriding plate. Trench-perpendicular profiles are taken through the middle of the model, at $y = 0$, of the interseismic horizontal surface velocity components, trench-perpendicular (a) and trench-parallel (b), respectively, for models with a contrast in the E value of the overriding plate (10 GPa near-trench, 100 GPa in the far-field) for different trench-contrast distances.

interseismic phase is linear and thus increases by the same, small amount. Overall, the presence and location of the mechanical contrast in the overriding plate has little effect on stressing rates on locked asperities.

4.7 Megathrust locking pattern affects the detectability of hurdles and contrasts

To assess the effect of a contrast on interseismic velocities in areas of low interplate locking, such as northern Peru and Ecuador (Nocquet *et al.* 2017; Herman & Govers 2020), we run two simulations in which the two intermediate asperities are removed, leaving three total asperities (2 lateral asperities centred 200 km from the centre of the middle one). We cut a profile halfway between the middle and outer asperities (at $y = 100$ km; Fig. 12). The profile through the former asperity (with three remaining asperities in the model) has lower trench-perpendicular velocities than the same profile through the asperity (model with five asperities), with a shallower slope of decrease in the near-trench portion of the overriding plate, but still with a clear hurdle in the form of a break in the slope at the location of the contrast in E (Fig. 12a). Trench-parallel velocities have a similar behaviour, except that velocities beyond the contrast are approximately identical.

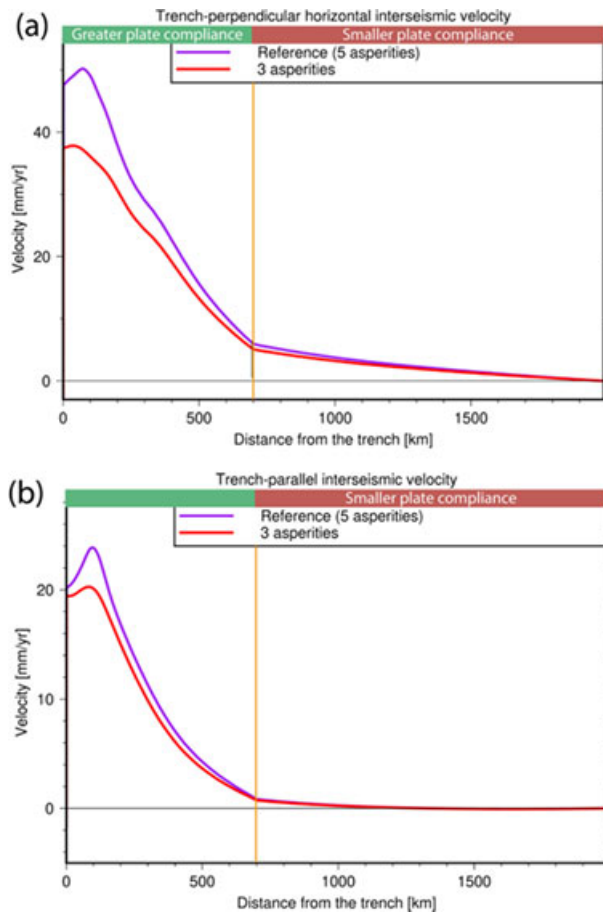


Figure 12. Sensitivity of interseismic velocities to the megathrust locking distribution. Trench-perpendicular profiles at $y = 100$ km (through the middle of one of the intermediate asperities, if present) of the two horizontal velocity components, trench-perpendicular (a) and trench-parallel (b), of interseismic velocities in a model with or without an intermediate asperity centred at $y = \pm 100$ km, halfway between the middle one (at $y = 0$) and each of the outer ones (at $y = \pm 200$ km).

4.8 Lateral thickness variation and sharpness of the mechanical contrast

In our models, a contrast in elastic moduli in an overriding plate of uniform thickness is a proxy for a general contrast in the plate's elastic compliance. We test the addition of a step increase in overriding plate thickness, doubling in thickness from 40 km at $x < 700$ km to 80 km at $x \geq 700$ km, to our reference model and to the model with a uniform E of 100 GPa. The trench-perpendicular interseismic velocity decreases ~ 30 per cent at the contrast while leaving the peak value unaffected, thus making its decrease with distance from the trench slightly steeper on the oceanward side of the contrast and more gradual on the beyond the contrast (Fig. 13). Trench-parallel velocities are unaffected by the thickness contrast. Heterogeneity in overriding plate thickness, and particularly a thinner arc region, likely contributes to the observed behaviour of interseismic surface velocities, but is not solely responsible for hurdle characteristics.

4.9 Effect of the ratio of the earthquake recurrence interval to the Maxwell time

The ratio $\frac{T}{\tau}$ of the earthquake recurrence interval T to the characteristic Maxwell relaxation time $\tau = \frac{\eta}{G}$ is an important property of

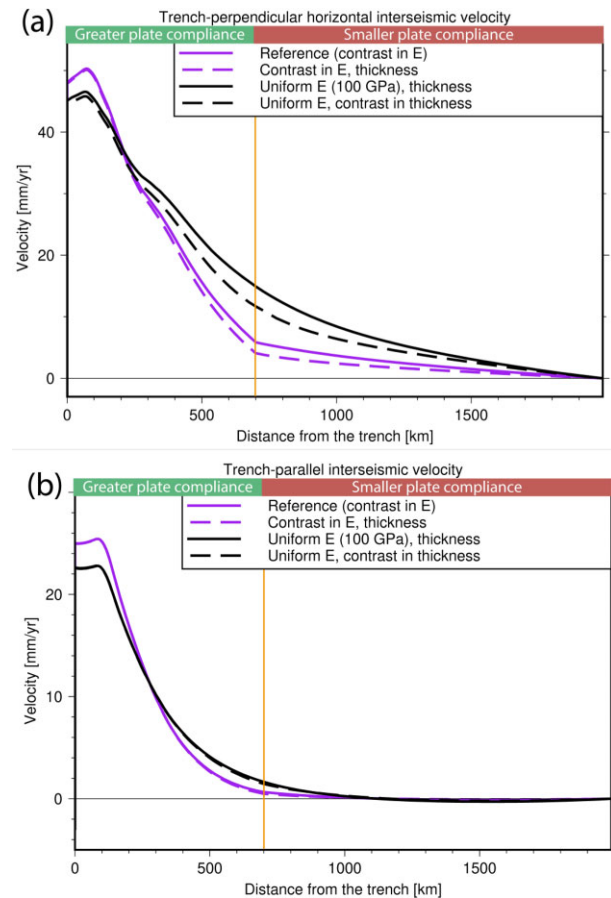


Figure 13. Sensitivity of interseismic velocities to the sharpness of the contrast within the overriding plate, and to thickness variations within the overriding plate. Trench-perpendicular profiles at $y = 0$ km of the two horizontal components, trench-perpendicular (a) and trench-parallel (b), of interseismic velocities in a model with or without a contrast in overriding plate thickness (40 km at $x < 700$ km, 80 km at $x > 700$ km). In both models there is the same contrast in overriding plate elastic moduli: the thinner portion of the plate has $E = 50$ GPa and the thicker one $E = 250$ GPa.

the megathrust system. In fact, it determines to what extent coseismic stresses have relaxed late in the cycle, and thus to what extent late interseismic motion reflects steady-state loading of the plate due to continued convergence and locking (Savage 1983). Higher $\frac{T}{\tau}$ ratios reduce the slope of trench-perpendicular velocities with distance from the fault trace in a simple 2-D dip-slip fault cutting across an elastic lithosphere overlying a Maxwell viscoelastic mantle (Wang *et al.* 2021). Our models so far use a $\frac{T}{\tau}$ ratio of 37.9, intermediate for the range of possible ratios observed for subduction zones worldwide and representing a case in which the stress changes due to coseismic slip and afterslip have relaxed late in the cycle (Govers *et al.* 2018).

We now explore the effect of reducing the $\frac{T}{\tau}$ ratio of our model with uniform elastic moduli throughout ($\nu = 0.25$, $E = 100$ GPa in the overriding plate and elsewhere), while keeping the convergence rate and earthquake size constant. Fig. 14 shows the interseismic velocity profiles for the model with the reference model viscosity of 10^{19} Pa·s (black line, same model and curves as in Figs 8, 9 and 13), and for alternative models with higher viscosities (i.e. longer relaxation times and smaller $\frac{T}{\tau}$) of the viscoelastic mantle. The resulting interseismic model velocities decrease more steeply with distance

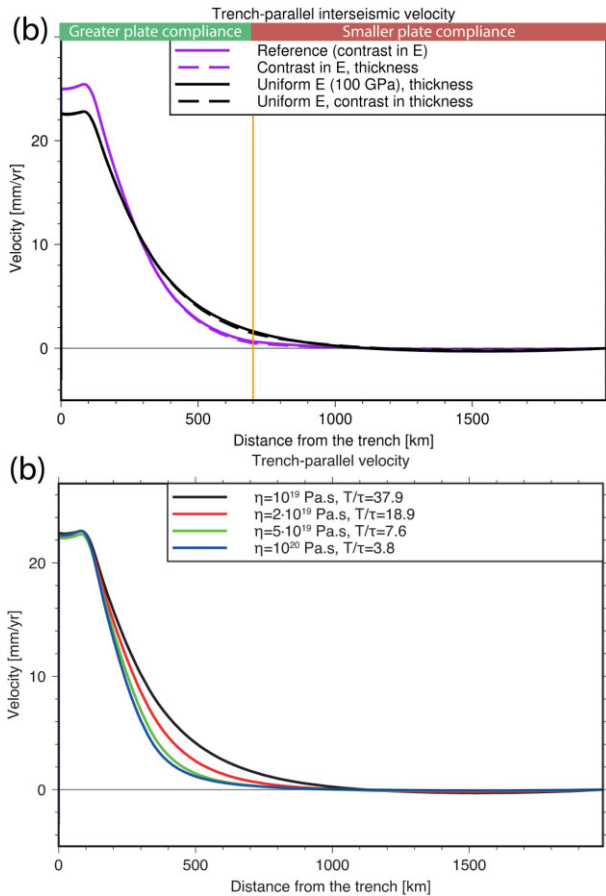


Figure 14. Sensitivity of interseismic velocities to the earthquake recurrence time T relative to the characteristic stress relaxation time (‘Maxwell time’) τ of the viscoelastic asthenosphere. Trench-perpendicular profiles at $y = 0$ km of the two horizontal components, trench-perpendicular (a) and trench-parallel (b), of interseismic velocities in models with an overriding plate without a contrast (uniform E of 100 GPa) and different values of $\frac{T}{\tau}$.

from the trench with decreasing $\frac{T}{\tau}$. The effect is particularly significant for the trench-perpendicular component. When the $\frac{T}{\tau}$ ratio is halved to 18.9, the effect is limited and the trench-perpendicular velocities still decrease shallowly with distance. However, further reducing $\frac{T}{\tau}$ makes the slope at intermediate-field distances even steeper, and particularly $\frac{T}{\tau} < 10$ makes the velocity 700 km away from the trench equal to or lower than 25 per cent of the peak value. This indicates that, for a sufficiently long Maxwell time relative to the earthquake recurrence interval, the hurdle behaviour exhibited by observed trench-perpendicular velocities may be explained without invoking a contrast in the compliance of the overriding plate. We further discuss the viability and implications of such explanation in Section 5.2.

5 DISCUSSION AND IMPLICATIONS

5.1 Scope and limitations of our study

We re-evaluate published interseismic GNSS velocity observations along three subduction margins: the Peru–Chile Trench (South America), the Sunda Trench (Sumatra, Java) and the Japan Trench (Hokkaido and northern Honshu). In South America, our analysis, not hampered by marine basins, yields the most continuous sampling of the kinematics in the overriding plate. The analysis will

need to be extended to other convergent margins before we can conclude that hurdles, breaks in the interseismic velocity gradient, are global features of megathrust margins. Still, with three out of the three margins showing hurdles, we think that we have a basis to hypothesize a more common feature that mechanically separates the deforming margin from a semi-stable overriding plate interior.

Our mechanical models are generic in their geometry, earthquake cycle, and mechanical properties. Further work will be needed to model the specific contribution of regional rheological makeup and active deformation structures to interseismic velocities. It might also be important to include radial elasticity variations and the sphericity of the Earth. Radially varying elasticity decreases does not affect far-field velocities (Pollitz *et al.* 2011a, b; see also Section 4.3). Sphericity was shown to have a negligible effect on modelled coseismic horizontal displacement due to thrust faulting at distances of 0–5000 km from the trench (Nostro *et al.* 1999). Trubienko *et al.* (2013) showed that interseismic displacement, normalized by the coseismic, 700 km from the trench has the same slope towards the end of the cycle, regardless of sphericity, indicating that interseismic velocities at the end of the cycle should also be hardly affected.

5.2 Role of the maxwell time in relation to the earthquake recurrence interval

As we show in Section 4.9, low values (broadly below 10) of the $\frac{T}{\tau}$ ratio cause the velocities to decrease more steeply with distance from the trench. In that case, coseismic stresses have not fully relaxed before the next earthquake occurs, and as a result viscoelastic model results become similar to those of fully elastic models. This effect is consistent with the results of the simple 2-D models of Wang *et al.* (2021) and of the earthquake cycle models of Li *et al.* (2015) and Trubienko *et al.* (2013). It is also analogous to model results showing that shorter recurrence times lead to greater localization of interseismic deformation around strike-slip faults (Zhu *et al.* 2020) and, conversely, that recurrence times that are long, compared to relaxation times, lead to substantial deviation between the deformation pattern of viscoelastic and of elastic models (Hetland & Hager 2005). Trubienko *et al.* (2013) explain the spatial distribution of interseismic velocities in two transects, through central Sumatra and the Malay peninsula and through northern Honshu in Japan, using an earthquake cycle model with a uniform elastic overriding plate. Their model uses a plane-strain approximation, a Burgers viscoelastic rheology for the mantle with a steady-state (Maxwell) viscosity $\eta = 3 \cdot 10^{19}$ Pa.s, asthenospheric elastic parameters from PREM (Dziewonski & Anderson 1981; giving $G \approx 68$ GPa and $\nu \approx 0.28$ in the asthenosphere), and a return period of 170 yr. Their $\frac{T}{\tau}$ is thus ~ 7.2 , accounting for the fact that τ is $3 \frac{1-\nu}{1+\nu} \frac{\eta}{G}$ higher in the plane strain regime (Melosh & Raefsky 1983). Li *et al.* (2015) similarly reproduce interseismic velocities in the North Chile portion of the Andean subduction zone using a uniform overriding plate, with a viscosity of 4×10^{19} Pa.s in the Maxwell viscoelastic mantle wedge and an earthquake cycle duration of 200 yr, resulting in a $\frac{T}{\tau}$ of ~ 10.1 .

Li *et al.* (2015) and Trubienko *et al.* (2013) do not incorporate finite gradients in slip deficit downdip of the locked interface and instead impose slip deficit to sharply transition from non-zero to zero at the downdip end of the megathrust. A sharp transition in slip deficit is physically unlikely (Herman & Govers 2020) and precludes the occurrence of the intermediate-depth afterslip (down to at least 80 km depth) that has been inferred from geodetic and seismological observations (Diao *et al.* 2014; Sun *et al.* 2014; Yamagiwa *et al.*

2015; Hu *et al.* 2016; Freed *et al.* 2017). The depth to which slip deficit accumulates is especially important, as Li *et al.* (2015) and Trubienko *et al.* (2013) show that greater locking depths producing larger intermediate-field and far-field velocities. These studies rely on shallow locking depths to reproduce interseismic velocities. Furthermore, when inverting observations, Li *et al.* (2015) do not apply a model spin-up, necessary to obtain viscous stresses and strain rates consistent with the long-term repetition of the earthquake cycle. As Li *et al.* (2015) point out, the spin-up would increase horizontal velocities, particularly in the intermediate-field (100–300 km from the trench), decreasing their trench-perpendicular slope. Therefore, the steepness of the decrease in interseismic velocities with distance from the trench is overestimated for a given $\frac{T}{\tau}$ ratio in the models of Li *et al.* (2015) and Trubienko *et al.* (2013). Nevertheless, their results suggest that low $\frac{T}{\tau}$ ratios might explain the apparent hurdle behaviour of interseismic velocities in the absence of contrasts in the compliance of the overriding plate.

Models of post-seismic relaxation following the 2004 Sumatra–Andaman earthquake, using Burgers rheologies for the asthenospheric mantle, consistently indicate steady-state viscosities of $\sim 10^{19}$ Pa-s, corresponding to a Maxwell time τ of ~ 5 yr (Hu & Wang 2012; Broerse *et al.* 2015; Qiu *et al.* 2018), while the recurrence interval for an earthquake of similar size has been estimated to be between 174 and 600 yr (Gahalaut *et al.* 2008; Meltzner *et al.* 2010; Van Veen *et al.* 2014), yielding $\frac{T}{\tau}$ ratios of 34.8–120. For the Chilean convergent margin, Klein *et al.* (2016) and Li *et al.* (2018) invert post-seismic GNSS observations in the few years (5 and 8, respectively) following the 2010 Maule earthquake, using a Burgers or Maxwell viscoelastic rheology, and consistently find Maxwell viscosities of $5\text{--}6 \times 10^{18}$ Pa-s in the continental asthenosphere under the Andes, corresponding to Maxwell times of 2.4–3.0 yr. Aron *et al.* (2015) estimate the return period as between 84 and 178 yr, which would put $\frac{T}{\tau}$ in the 28.0–74.2 range. In the Japan subduction zone, simultaneous inversions of GNSS time-series following the 2011 Tohoku earthquake into afterslip and viscoelastic relaxation parameters, using Burgers or non-linear flow law-based viscoelastic rheologies for the asthenosphere, indicate that the steady-state viscosity of the mantle wedge is in the range of $4\text{--}10 \times 10^{18}$ Pa-s (Agata *et al.* 2019; Muto *et al.* 2019; Fukuda & Johnson 2021). This corresponds to Maxwell relaxation times of 2.0–5.0 yr and is in agreement with the results of the inversion of gravity data into viscous relaxation parameters only by Cambiotti (2020). The recurrence interval T for events similar to the 2011 Tohoku-oki earthquake is ~ 600 yr (Satake 2015), which puts the $\frac{T}{\tau}$ ratio in the 120–300 range. The ratios (12.1 and 7.2, respectively) used by Trubienko *et al.* (2013) and Li *et al.* (2015) are thus below the low end of the realistic range. Our models reproduce the hurdle-like response for low ratios of $\frac{T}{\tau}$ (section 4.9). Still, higher ratios are more realistic for the active margins that we investigate, and our model results show that hurdle behaviour is not reproduced with uniform high $\frac{T}{\tau}$ ratios (mantle viscosities in line with the majority of post-seismic studies) combined with uniform elastic compliancy of the overriding plate (Sections 4.2 and 4.4). This argues for compliancy contrasts in the overriding plate.

5.3 Tectonic significance of a mechanical contrast

Klein *et al.* (2016) suggest that stiff cratonic backarc lithosphere in central Argentina affects horizontal and vertical post-seismic surface velocities following the Maule earthquake. Li *et al.* (2018)

invert post-seismic displacements, including in the far field, following the Maule earthquake into rheological structures of the upper mantle, finding strong evidence for a stiff (elastic, or viscoelastic with high viscosity) cratonic lithospheric root beneath central Argentina. Seismic data also indicate that the Andean lithosphere has very thick crust and warm lithospheric mantle that contrast with thinner (but still thick) cratonic crust underlain by cold, stiff lithospheric mantle farther to the east, from Venezuela to central Argentina (Chulick *et al.* 2013). This juxtaposition represents a significant contrast in lithospheric averages of the compliance. The hurdle location that we inferred from the GNSS velocities agrees with the tectonic boundary (Section 2.5, Fig. 6a). Immediately to the south of the Central Andes, around 30°S, the trench-perpendicular hurdle coincides with different terrane and active tectonic boundaries (Fig. 6a; Ramos 1988, 1999). In particular, it is located between the eastern front of the active Andean Precordillera fold-and-thrust belt (Ortiz & Zambrano 1981; Baldis *et al.* 1982) and the western margin of the Rio de la Plata craton (Álvarez *et al.* 2012), within a mountain range (the Sierras Pampeanas) characterized by active reverse faults and lateral contrasts in crustal thickness and layering (Perarnau *et al.* 2012) (Fig. 6a). The eastern edge of the Andes as marked by active faults correlates spatially with the western edge of the distinct, stable, largely cratonic interior of the South America Plate. Thus, the general but imperfect coincidence of the hurdle with the active backthrust, where present, is consistent with the hurdle being determined by a contrast in compliance that occurs with different amplitudes and different depth dependences along the orogen.

In Sunda, the overriding plate is a set of Palaeozoic–Cenozoic accreted terranes (Hall *et al.* 2009). We are unaware of independent proof that Sundaland is mechanically stiffer than the Sumatra forearc. However, a significant crustal contrast exists across the Meratus palaeosuture in Java (Fig. 6b; Haberland *et al.* 2014). Contrasts may also exist across two major structural boundaries. The first of these is peninsular Malaysia's Bentong–Raub suture zone, which separates the Sibumasu terrane to its southwest from the Indochina terrane (Metcalfe 2000). The second boundary is the Medial Sumatra Tectonic Zone, which separates the Sibumasu terrane to the northeast from the West Sumatra block and the overlying Woyla accretionary complex and volcanic arc (Hutchison 1994, 2014; Barber 2000; Barber *et al.* 2005) and which largely coincides with the strike-slip Sumatran Fault in central and northern Sumatra. Simons *et al.* (2007) used GNSS data to identify the approximate boundaries of the interseismically non-deforming part of the Sundaland block (Michel *et al.* 2001); its internal (south and west) boundary aligns roughly with geological suture boundaries. On the other hand, estimates from coherence between gravity and topography show no evidence of a block in the interior of the plate with higher T_e than the forearc region (Audet & Bürgmann 2011; Shi *et al.* 2017).

To explain the steep spatial gradient near the trench in horizontal interseismic velocities in Hokkaido, Japan, Itoh *et al.* (2019, 2021) proposed and modelled the effect of a compliant lithosphere in the volcanic arc and backarc, in contrast with a less compliant forearc, as evidenced by temperature, heat flux and seismic wave attenuation (Tanaka *et al.* 2004; Wang & Zhao 2005; Katsumata *et al.* 2006; Wada & Wang 2009; Liu *et al.* 2013; Kita *et al.* 2014). However, in the model of Itoh *et al.* (2019), velocities are restricted by the fixed landward edge of the domain, which localizes shortening and shearing in the compliant material. We propose that velocities are instead restricted by the contrast between the compliant arc and backarc and the less compliant material farther from the trench, in the Sea of Japan and beyond. The Sea of Japan is a Miocene

backarc basin of the Japan and southern Kurile subduction zones. It is inactive (Karig 1974), having ceased extending around 14 Mya (Tatsumi *et al.* 1989), and is likely less compliant than the Japan arc. The Amurian–Okhotsk Plate boundary follows the sea’s eastern margin (Seno *et al.* 1996; Fig. 6c). The plate boundary mechanically decouples these plates in the long term, but they are coupled during most of the earthquake cycle. The lack of GNSS observations in the Sea of Japan prevents us from determining where exactly the compliance contrast occurs and whether creep along the plate boundary further affects velocities.

5.4 Compliance contrasts in a rheological and geodynamic context

As stated in Section 4.4, our model results suggest that interseismic velocities might necessitate a larger contrast in interseismic compliance within the overriding plate than can be provided by realistic elastic parameters. Concretely, the Young’s modulus needs to be high enough in the portion of the plate between the trench and the hurdle as to transmit substantial coseismic displacement to the far-field, and low enough in the far-field interior of the plate as to not exceed plausible values. The portion of the plate between the trench and hurdle must thus transition from its greater coseismic compliance, dictated by elastic properties, to lesser compliance in the interseismic period. This transition might be related to viscous creep of the lower crust and upper mantle (Bürgmann & Dresen 2008), which reduces flexural rigidity (Ranalli 1995), and likely also compliance, over time after loading. Low effective elastic thickness is thought to indicate departure from purely elastic rheology, such as due to high temperatures, inherited weak zones, or high horizontal stresses (Burov & Diament 1995), which are likely to occur in the thermomechanically young lithosphere at convergent boundaries. The increased water content at subduction zones also contributes to departure from elasticity by decreasing the viscosity (Kirby 1983; Chopra & Paterson 1984; Hirth & Kohlstedt 1996; Dixon *et al.* 2004) and lower plastic strength (Blacic & Christie 1984; Mainprice & Paterson 1984) of the lower crust and upper mantle. Geodynamic, petrological–thermomechanical numerical modelling of subduction shows that brittle-plastic rheological weakening by both fluids and melts plays an important role in the evolution of the subduction zone and in the development of the volcanic arc and the backarc region (Gerya & Meilick 2011). Increased viscosity of the upper mantle under cratons, such as caused by water depletion (Dixon *et al.* 2004), might also contribute to the effective compliance contrast between the lithosphere–asthenosphere system of the plate interior and that of the near-margin region.

5.5 Geodetically stable parts of overriding plates?

Observations of significant coseismic displacements thousands of km away from the megathrust rupture called into question the concept of an undeforming (rigid) reference plate (Vigny *et al.* 2005; Wang *et al.* 2011; Pollitz *et al.* 2011a; see also Section 4.1). Our analysis suggests indeed that small but non-zero interseismic velocities and velocity gradients extend beyond the hurdles, and this presents a challenge for defining a reference on a geodetic observation timescale. On timescales spanning the time needed to complete a seismic catalogue on the megathrust (tens to thousands of years, e.g. Ward 1998a, b), it is possible that the net accumulated strain is zero, that is there may exist a fully rigid reference on geological timescales.

5.6 Role of major faults in the Central Andes

As discussed in Section 2.6, previous studies observe and explain the spatial behaviour of interseismic velocities, in the context of the Central Andes, as a result of shortening on backthrusts (Norabuena *et al.* 1998; Bevis *et al.* 2001; Brooks *et al.* 2003, 2011; Kendrick *et al.* 2006; Weiss *et al.* 2016; McFarland *et al.* 2017; Shi *et al.* 2020). Quantitative models in these studies use either a uniform elastic half-space, or apply zero-displacement boundary conditions close to the backthrust. Both choices artificially restrict interseismic velocities to the near-trench region, compared to using elastic plates overlying viscoelastic mantle and extending well into the far-field. To explain the observed interseismic surface velocities, most of the studies also need basal thrusts that are more spatially extensive than supported by geological evidence (see Section 2.6). However, localized shortening has a more regional role in determining specific trench-perpendicular velocities, particularly in backarc thrust belts and basal faults and in the interior of active-margin orogens. For instance, when these faults only decouple the shallow lithosphere, they may locally cause discontinuities and increased spatial gradients, without affecting the near-trench portion of the velocity field (Shi *et al.* 2020). Major, creeping strike-slip faults likely cause large local gradients in trench-parallel velocities, and can localize trench-parallel velocities in a way not necessarily related to the presence of a contrast (Section 2.6). Nevertheless, contrasts in lithologies and plate thickness, responsible for hurdles, might also result from continued motion along strike-slip faults. In turn, the presence of such contrasts might localize lateral motion into narrow fault zones.

6 CONCLUSIONS

Interseismic GNSS velocities from the three studied subduction zones show a broadly linear decrease of the trench-perpendicular velocity with distance from the trench up to what we define as the hurdle, located at variable distances less than 1000 km. Beyond the hurdle, trench-perpendicular velocities are near-zero (less than $\sim 5 \text{ mm yr}^{-1}$) extending over thousands of kilometres away from the trench. Trench-parallel velocities are in some cases affected by presence of strike-slip faults (Sumatra), or are insignificant because of head-on convergence (Japan, Java). In South America, however, they generally also decrease steeply with distance, up to a hurdle. The hurdle roughly coincides with the trench-perpendicular hurdle or is located up to several tens of km closer to the trench. This interseismic deformation restricted to the near-trench region contrasts with significant coseismic displacements that were recorded beyond these hurdles during the large 2004 Sumatra, 2010 Maule and 2011 Tohoku earthquakes.

The location of the hurdle in observed trench-perpendicular velocities often coincides with major tectonic or geological boundaries separating a plate margin region from a distinct, and likely more rigid, plate interior. In South America the trench-perpendicular hurdle generally follows the eastern edge of the orogen, coinciding with the western margin of the cratonic lithosphere and the eastern margin of the accreted, deformed terranes at the active plate margin. In Sumatra, the hurdle follows the Medial Sumatra Tectonic Zone. Off the shore of northern Honshu and Hokkaido in Japan, the hurdle probably coincides with the boundary between the backarc region of the islands, to the east, and the inactive backarc basin and Amur Plate interior to the west.

Our numerical modelling results show that a contrast in overriding plate compliance can reproduce the steep, largely linear near-trench decrease in trench-perpendicular velocities with distance. In

our models, this decrease ends abruptly at the location of the contrast, that is at the hurdle. The value of elastic moduli on either side of the contrast determines the contrast amplitude and thus affects the intensity of the hurdle behaviour: a weaker contrast steepens the near-trench slope and/or makes the far-field slope more shallow. Strengthening the contrast by decreasing the near-trench elastic moduli has a greater effect on trench-perpendicular velocities than increasing the far-field moduli, but higher far-field moduli are still important in introducing and defining the hurdle behaviour. In contrast, trench-parallel velocities are controlled only by the near-trench elastic moduli and decrease more gradually. The steep decrease in the first couple of hundred km from the trench defines an apparent hurdle that, for the values tested in our models, is closer to the trench than the location of the contrast. The distance between the two depends on the specific elastic moduli and the location of their contrast.

The presence and location of compliance contrasts does not significantly affect the rate at which shear traction increases on the asperities in our models. The width of the zone where interseismic strain primarily accumulates, roughly between the coastline and the hurdle, likely does not generate significant variations in megathrust earthquake magnitude or recurrence interval. Velocities in portions of the subduction zone with little slip deficit, that is little apparent interplate coupling on the megathrust, have lower near-trench trench-perpendicular gradients but otherwise similar behaviour, particularly in the trench-perpendicular components. Their near-trench trench-parallel components exhibit more complex gradients depending on location with respect to the fully coupled asperities and the direction of trench-parallel, far-field interplate motion.

SUPPORTING INFORMATION

Supplementary data are available at [GJI](https://doi.org/10.1002/gji.1879) online.

Figure S1. Decomposition of interseismic velocities in the South America Plate reference into trench-perpendicular and trench-parallel velocities.

Figure S2. Decomposition of interseismic velocities in the Sunda Plate reference into trench-perpendicular and trench-parallel velocities.

Figure S3. Decomposition of Honshu and Hokkaido interseismic velocities in the Okhotsk Plate reference into trench-perpendicular and trench-parallel velocities.

Figure S4. Gaussian kernel radius for the weighting of trench-perpendicular (x) and trench-parallel (y) velocities in constructing the local covariance functions at each anchor point in South America. Black dots denote GNSS observation points. As the kernel is defined based on the distance to natural neighbours of the anchor point, densely sampled areas (often near-trench) have a narrow weighting kernel, while sparsely sampled areas have a wide weighting kernel. In some areas a low signal-to-noise may lead to a kernel radius that is larger than the natural neighbourhood, to prevent relatively large nugget values, compared to the covariance function variance.

Figure S5. Estimated local covariance (exponential) parameters: range and variance, for trench-perpendicular (x) and trench-parallel (y) velocities in South America. Range (in meters) describes the decay of the correlation with distance, variance denotes the local observation variance (in $\text{mm}^2 \text{yr}^{-2}$). The variance is generally larger if the observation changes much within a natural neighborhood (roughly in between observation points) or in some cases, when the kernel radius is large because of a low signal-to-noise ratio.

Figure S6. Gaussian kernel radius for the weighting of trench-perpendicular (x) and trench-parallel (y) velocities in constructing the local covariance functions at each anchor point in Southeast Asia. Black dots denote GNSS observation points. As the kernel is defined based on the distance to natural neighbours of the anchor point, densely sampled areas (often near-trench) have a narrow weighting kernel, while sparsely sampled areas have a wide weighting kernel. In some areas a low signal-to-noise ratio may lead to a kernel radius that is larger than the natural neighbourhood, to prevent relatively large nugget values, compared to the covariance function variance.

Figure S7. Estimated local covariance function (exponential) parameters: range and variance, for trench-perpendicular (x) and trench-parallel (y) velocities in Southeast Asia. Range (in metres) describes the decay of the correlation with distance, variance denotes the local observation variance (in $\text{mm}^2 \text{yr}^{-2}$). The variance is generally larger if the observation changes much within a natural neighbourhood (roughly in between observation points) or in some cases, when the kernel radius is large because of a low signal-to-noise ratio.

Figure S8. Gaussian kernel radius for the weighing of trench-perpendicular (x) and trench-parallel (y) velocities in constructing the local covariance functions at each anchor point in Japan. Black dots denote GNSS observation points. As the kernel is defined based on the distance to natural neighbours of the anchor point, densely sampled areas (often near-trench) have a narrow weighting kernel, while sparsely sampled areas have a wide weighting kernel.

Figure S9. Estimated local covariance function (exponential) parameters: range and variance, for trench-perpendicular (x) and trench-parallel (y) velocities in Japan. Range (in metres) describes the decay of the correlation with distance, variance denotes the local observation variance (in $\text{mm}^2 \text{yr}^{-2}$). The variance is generally larger if the observation changes much within a natural neighbourhood (roughly in between observation points) or in some cases, when the kernel radius is large because of a low signal-to-noise ratio. The latter is the case for the trench-parallel variances, as the reported uncertainties are larger than the parallel signal. Still, we find a consistent parallel signal in most of the domain, which suggests that the error is overestimated.

Figure S10. Uncertainty estimates (1 standard deviation) from the local ordinary kriging, trench-perpendicular and trench-parallel directions, for interseismic velocities in South America. In kriging uncertainties depend on both (local) variance, as well as on observation variance. In our implementation of local ordinary kriging uncertainties are large in areas with large gradients (especially when natural neighbours are relatively far apart), and small in areas with small gradients, see Fig. 3 in the main text for the interpolated field. Circles denote the GNSS velocity uncertainties.

Figure S11. Uncertainty estimates (1 standard deviation) from the local ordinary kriging, trench-perpendicular and trench-parallel directions, for interseismic velocities in Southeast Asia. In kriging uncertainties depend on both (local) variance, as well as on observation variance. In our implementation of local ordinary kriging uncertainties are large in areas with large gradients (especially when natural neighbours are relatively far apart), and small in areas with small gradients, see Fig. 4 in the main text for the interpolated field. Circles denote the GNSS velocity uncertainties.

Figure S12. Uncertainty estimates (1 standard deviation) from the local ordinary kriging, trench-perpendicular and trench-parallel directions, for interseismic velocities in Japan. In kriging uncertainties depend on both (local) variance, as well as on observation

variance. In our implementation of local ordinary kriging uncertainties are large in areas with large variability in observed velocities and large distances between observations, and small in areas with dense data coverage and small variability in observed velocities. See Fig. 5 in the main text for the interpolated field. Circles denote the GNSS velocity uncertainties.

Figure S13. Results of the analysis of velocities in Japan, expressed in an Amur Plate reference frame, rather than an Okhotsk Plate reference frame as in Fig. 5 in the main text. The maps show interpolated trench-perpendicular (positive landward) and trench-parallel (positive left-lateral) velocity fields with 95 per cent confidence-interval location of the hurdle, together with active faults in green from GEM (Styron & Pagani 2020). Coastlines are in black and arrows show the interplate convergence direction between the Pacific Plate and the Amur Plate (Kreemer *et al.* 2014). Below, we show selected trench-perpendicular profiles, in Honshu and Hokkaido, on the landward side of the Japan Trench, along the profile lines traced in the maps. The velocity profiles show both interpolated velocity components with 1 standard deviation uncertainty (transparent bands), and the velocity components at GNSS stations within the swath with 1 standard deviation error bars. Note that the interpolated velocities are based on all GNSS velocity estimates, and not only those shown in the swath for reference. Vertical green and orange lines and bands outline estimated hurdle distances with 95 per cent confidence intervals.

Figure S14. Isometric projection of the finite element mesh used in our numerical models.

Figure S15. Trench-perpendicular profiles at $y = 0$ through the interseismic horizontal surface velocity components, trench-perpendicular (a) and trench-parallel (b), respectively, for a model with elastic moduli according to the vertical profile of PREM (Dziewonski & Anderson 1981) or constant, uniform values. In the slab, E is 100 GPa and ν is 0.25 in both models.

Figure S16. Trench-perpendicular profiles at $y = 0$ through the interseismic horizontal surface velocity components, trench-perpendicular (a) and trench-parallel (b), respectively, for models with the same contrast in overriding plate E (30 GPa at $x < 700$ km, 150 GPa at $x > 700$ km), the same overriding plate G (87.5 GPa) and ν (0.2) at $x > 700$ km, and an overriding plate G at $x < 700$ km of either 12.5 GPa (same $\nu = 0.2$ as at $x > 700$ km, same 1:7 ratio to far-field G as between near-field and far-field E) or 10.71 GPa ($\nu = 0.4$, 1:8.17 ratio to far-field G).

Figure S17. Plot of average traction in the down-dip direction (interface-parallel, along parallel lines on the interface intersecting the trench at right angles) on the central asperity on the megathrust interface, through time over an earthquake cycle, in models with different horizontal distance between the trench and the contrast in E (10 GPa near-trench, 100 GPa elsewhere). The earthquake on the middle asperity happens at time 0, while the earthquakes on the intermediate and external asperities happen at time 20 and 40 yr, respectively.

Table S1. Overview of the collection of horizontal velocities for the South American margin, including the source, the observational period, the reference frame in which the velocities are reported. ^aWe make use of the velocities expressed by Kreemer *et al.* (2014), where all previously published velocities have been transformed to IGS08 in a global inversion to estimate rotation and translation rates based on common sites. ^bWe apply the rotation pole 25.4S, 124.6 W, 0.11° Myr⁻¹ as provided in Métois *et al.* (2012) to transform back to ITRF2005. ^cWe apply the rotation pole 18.83S, 132.21 W, 0.121° Myr⁻¹ as provided by the authors to transform the published plate referenced velocities back to ITRF2008. ^dWe

apply the rotation pole 18.66S, 132.72 W, 0.118° Myr⁻¹ as provided in the supplementary information of Villegas-Lanza *et al.* (2016) to transform back to ITRF2008. ^eWeiss *et al.* (2016) use a South America Plate reference, constructed with 44 cGPS sites, mostly located in Brazil, without a prior global solution. ^fWeiss *et al.* (2016) apply a post-seismic correction of the 2007 Tocopilla M_w 7.7 earthquake to the velocity estimates, by removing an empirically estimated coseismic step and post-seismic decay function. ^gMcFarland *et al.* (2017) used the ITRF2008 South American Plate motion model (Altamimi *et al.* 2012), which we subsequently use to transform back to ITRF2008. ^hWe exclude sites SURY, RAS, PRMA, LSJ1, SPBP, NXRA, LDO, LPLN, for which observed velocities are anomalously high in comparison to neighbouring sites.

Table S2. Overview of the collection of horizontal velocities for the Sunda margin, including the source, the observational period, the reference frame in which the velocities are reported. ^aWe make use of the velocities expressed by Kreemer *et al.* (2014), where all previously published velocities have been transformed to IGS08 in a global inversion to estimate rotation and translation rates based on common sites. ^bSites from the 1991–2001 have not been affected by major earthquakes, ^{c,d} and we do not use the data from the 2001–2007 and 2002–2006 tables in areas affected by the 2004 Sumatra–Andaman earthquake and the 2005 Nias earthquakes. ^eWe use the table with exclusion periods for individual sites to be able to filter sites that are potentially affected by post-seismic transients. ^fVelocities obtained from data after the 2006 M_w 7.7 earthquake in west Java has been corrected for coseismic offsets and post-seismic transients using a best-fitting viscoelastic model. ^gPublished velocities in Koulali *et al.* (2017) are expressed in a Sunda Plate reference, we use the Euler pole that we received from the authors to express velocities in ITRF2008. Euler pole parameters: longitude 81.07° W, latitude 32.66° N, angular velocity 0.435924° Myr⁻¹.

Table S3. Overview of the collection of horizontal velocities for the Japan margin in the pre-2011 Tohoku earthquake period, including the source, the observational period, the reference frame in which the velocities are reported. ^aWe make use of the velocities expressed by Kreemer *et al.* (2014), where all previously published velocities have been transformed to IGS08 in a global inversion to estimate rotation and translation rates based on common sites. ^bHashimoto *et al.* (2009) have corrected for transients of the 1994 Sanriku earthquake. ^cWe exclude sites that have velocity estimates based partly on post-2011 Tohoku data.

Video S1. Animation showing interpolated velocities, their uncertainties, and estimated hurdle locations, where available, along trench-perpendicular profiles at different locations all along the Peru–Chile Trench in South America. Some of these profiles are shown as panels A–D in Fig. 3.

Video S2. Animation showing interpolated velocities, their uncertainties and estimated hurdle locations, where available, along trench-perpendicular profiles at different locations all along the Sunda Trench in Southeast Asia. Some of these profiles are shown as panels A–C in Fig. 4.

Video S3. Animation showing interpolated velocities, their uncertainties and estimated hurdle locations, where available, along trench-perpendicular profiles at different locations all along the Japan Trench in central and northern Japan. Some of these profiles are shown as panels A and B in Fig. 5.

Please note: Oxford University Press is not responsible for the content or functionality of any supporting materials supplied by the authors. Any queries (other than missing material) should be directed to the corresponding author for the paper.

ACKNOWLEDGMENTS

This work was funded by Dutch Research Council (NWO) grant ALWGO.2017.007. We thank the following people for providing additional background information for the velocity data sets that we have used in this study: Laura Sánchez, Jean-Mathieu Nocquet, Corné Kreemer and Achraf Koulali. Insightful reviews by Kelin Wang, Emilie Klein, Rocco Malservisi and two anonymous reviewers contributed significantly to the improvement of earlier versions of the paper. We thank editor Kosuke Heki for his constructive evaluation and support.

Author contributions following the CRediT taxonomy: Conceptualization: R. Govers, T. Broerse, M. D'Acquisto. Methodology: T. Broerse, M. D'Acquisto. Software: R. Govers, T. Broerse. Validation: T. Broerse, M. D'Acquisto. Formal Analysis: M. D'Acquisto, T. Broerse. Investigation: M. D'Acquisto, C. P. Marsman. Resources: R. Govers. Data Curation: M. D'Acquisto. Writing-Original Draft: M. D'Acquisto, R. Govers, T. Broerse, C. P. Marsman. Writing-Review & Editing: M. D'Acquisto, T. Broerse, R. Govers, C. P. Marsman. Visualization: M. D'Acquisto, T. Broerse. Supervision: R. Govers. Project Administration: R. Govers. Funding Acquisition: R. Govers.

The mesh generator program Gmsh (Geuzaine & Remacle 2009) was used to make the finite element meshes for the numerical models. The MATLAB software platform (MATLAB 2018), the Generic Mapping Tools (Wessel *et al.* 2019), and the Adobe Illustrator program (Adobe Inc. 2019) were used for visualization.

DATA AVAILABILITY

The model output files that we used for the figures of this paper are digitally stored in the Yoda repository of Utrecht University and are freely available under the CC-BY license at <https://doi.org/10.24416/UU01-6SC8XG>.

REFERENCES

- Adobe Inc., 2019. Adobe Illustrator (Version CC 2019 (23.0.3)), Retrieved from <https://adobe.com/products/illustrator>.
- Agata, R., Barbot, S. D., Fujita, K., Hyodo, M., Iinuma, T., Nakata, R., Ichimura, T. & Hori, T., 2019. Rapid mantle flow with power-law creep explains deformation after the 2011 Tohoku mega-quake, *Nat. Commun.*, **10**(1), 1–11.
- Altamimi, Z., Collilieux, X. & Métivier, L., 2011. ITRF2008: an improved solution of the international terrestrial reference frame, *J. Geod.*, **85**(8), 457–473.
- Altamimi, Z., Métivier, L. & Collilieux, X., 2012. ITRF2008 plate motion model, *J. geophys. Res.*, **117**(B7), doi:10.1029/2011JB008930.
- Alvarado, A. *et al.*, 2014. Active tectonics in Quito, Ecuador, assessed by geomorphological studies, GPS data, and crustal seismicity, *Tectonics*, **33**(2), 67–83.
- Alvarado, A. *et al.*, 2016. Partitioning of oblique convergence in the Northern Andes subduction zone: migration history and the present-day boundary of the North Andean Sliver in Ecuador, *Tectonics*, **35**(5), 1048–1065.
- Alvarado, P. & Ramos, V. A., 2011. Earthquake deformation in the north-western Sierras Pampeanas of Argentina based on seismic waveform modelling, *J. Geodyn.*, **51**(4), 205–218.
- Álvarez, O., Gimenez, M., Braitenberg, C. & Folguera, A., 2012. GOCE satellite derived gravity and gravity gradient corrected for topographic effect in the South Central Andes region, *Geophys. J. Int.*, **190**(2), 941–959.
- Aoki, I. & Takahashi, E., 2004. Density of MORB eclogite in the upper mantle, *Phys. Earth planet. Inter.*, **143–144**, 129–143.
- Apel, E. V., Bürgmann, R., Steblov, G., Vasilenko, N., King, R. & Prytkov, A., 2006a. Independent active microplate tectonics of northeast Asia from GPS velocities and block modeling, *Geophys. Res. Lett.*, **33**(11), doi:10.1029/2006GL026077.
- Aron, F., Cembrano, J., Astudillo, F., Allmendinger, R. W. & Arancibia, G., 2015. Constructing forearc architecture over megathrust seismic cycles: geological snapshots from the Maule earthquake region, Chile, *Bull. geol. Soc. Am.*, **127**(3–4), 464–479.
- Audet, P. & Bürgmann, R., 2011. Dominant role of tectonic inheritance in supercontinent cycles, *Nat. Geosci.*, **4**(3), 184–187.
- Balay, S. *et al.*, 2021a. *PETSc/TAO Users Manual (No. ANL-21/39-Revision 3.16)*. Argonne National Laboratory.
- Balay, S. *et al.*, 2021b. PETSc Web page. Retrieved 30 April 2022, from <https://petsc.org/>
- Balay, S., Gropp, W. D., McInnes, L. C. & Smith, B. F., 1997. Efficient management of parallelism in object oriented numerical software libraries, in *Modern Software Tools in Scientific Computing*, pp. 163–202, eds Arge, E., Bruaset, A. M. & Langtangen, H. P., Birkhäuser Press.
- Baldis, B. A., Beresi, M., Bordonaro, O. & Vaca, A., 1982. Síntesis evolutiva de la Precordillera Argentina, in *Proceedings of the 5th Latin American Congress of Argentine Geology*, Vol. IV, Servicio Geológico Nacional, Subsecretaría de Minería, Buenos Aires, Argentina, pp. 399–445.
- Barber, A. J., 2000. The origin of the Woyla Terranes in Sumatra and the late mesozoic evolution of the Sundaland margin, *J. Asian Earth Sci.*, **18**(6), 713–738.
- Barber, A. J., Crow, M. J. & Milsom, J., 2005. *Sumatra: Geology, Resources and Tectonic Evolution*, Geological Society of London.
- Bevis, M., Kendrick, E., Smalley, R., Brooks, B., Allmendinger, R. & Isacks, B., 2001. On the strength of interplate coupling and the rate of back arc convergence in the central Andes: an analysis of the interseismic velocity field, *Geochem. Geophys. Geosyst.*, **2**(11), doi:10.1029/2001GC000198.
- Bird, P., 2003. An updated digital model of plate boundaries, *Geochem. Geophys. Geosyst.*, **4**(3), doi:10.1029/2001GC000252.
- Blacic, J. D. & Christie, J. M., 1984. Plasticity and hydrolytic weakening of quartz single crystals, *J. geophys. Res.*, **89**(B6), 4223–4239.
- Blewitt, G., Kreemer, C., Hammond, W. C. & Gazeaux, J., 2016. MIDAS robust trend estimator for accurate GPS station velocities without step detection, *J. geophys. Res.*, **121**(3), 2054–2068.
- Bock, Y. *et al.*, 2003. Crustal motion in Indonesia from Global Positioning System measurements, *J. geophys. Res.*, **108**(B8), doi:10.1029/2001JB000324.
- Broerse, T., Riva, R., Simons, W., Govers, R. & Vermeersen, B., 2015. Postseismic GRACE and GPS observations indicate a rheology contrast above and below the Sumatra slab, *J. geophys. Res.*, **120**(7), 5343–5361.
- Brooks, B. A. *et al.*, 2011. Orogenic-wedge deformation and potential for great earthquakes in the central Andean backarc, *Nat. Geosci.*, **4**(6), 380–383.
- Brooks, B. A., Bevis, M., Smalley, R., Kendrick, E., Manceda, R., Lauria, E., Maturana, R. & Araujo, M., 2003. Crustal motion in the southern Andes (26°–36° S): do the Andes behave like a microplate?, *Geochem. Geophys. Geosyst.*, **4**(10), doi:10.1029/2003GC000505.
- Bürgmann, R. & Dresen, G., 2008. Rheology of the lower crust and upper mantle: evidence from rock mechanics, geodesy, and field observations, *Annu. Rev. Earth planet. Sci.*, **36**(1), 531–567.
- Burov, E. B. & Diament, M., 1995. The effective elastic thickness (T_e) of continental lithosphere: what does it really mean?, *J. geophys. Res.*, **100**(B3), 3905–3927.
- Cambiotti, G., 2020. Joint estimate of the coseismic 2011 Tohoku earthquake fault slip and post-seismic viscoelastic relaxation by GRACE data inversion, *Geophys. J. Int.*, **220**(2), 1012–1022.
- Chlieh, M., Avouac, J. P., Sieh, K., Natawidjaja, D. H. & Galetzka, J., 2008. Heterogeneous coupling of the Sumatran megathrust constrained by geodetic and paleogeodetic measurements, *J. geophys. Res.*, **113**(B5), doi:10.1029/2007JB004981.
- Chlieh, M., De Chabaliér, J. B., Ruegg, J. C., Armijo, R., Dmowska, R., Campos, J. & Feigl, K. L., 2004. Crustal deformation and fault slip during the seismic cycle in the North Chile subduction zone, from GPS and InSAR observations, *Geophys. J. Int.*, **158**(2), 695–711.

- Chopra, P. N. & Paterson, M. S., 1984. The role of water in the deformation of dunite, *J. geophys. Res.*, **89**(B9), 7861–7876.
- Christensen, N. I., 1996. Poisson's ratio and crustal seismology, *J. geophys. Res.*, **101**(B2), 3139–3156.
- Chulick, G. S., Detweiler, S. & Mooney, W. D., 2013. Seismic structure of the crust and uppermost mantle of South America and surrounding oceanic basins, *J. South Am. Earth Sci.*, **42**, 260–276.
- Cisneros, D. & Nocquet, J., 2011. Campo de velocidades del Ecuador, obtenido a través de mediciones de campañas GPS de los últimos 15 años y medidas de una red GPS permanente, Retrieved from: http://www.sirgas.org/fileadmin/docs/Cisneros_2010_Campo_velocidades_Ecuador_web.pdf
- Conn, A. R., Gould, N. I. M. & Toint, P. L., 2000. *Trust Region Methods*, SIAM.
- Delouis, B., Nocquet, J.-M. & Vallée, M., 2010. Slip distribution of the February 27, 2010 Mw = 8.8 Maule Earthquake, central Chile, from static and high-rate GPS, InSAR, and broadband teleseismic data, *Geophys. Res. Lett.*, **37**(17), doi:10.1029/2010GL043899.
- Diao, F., Xiong, X., Wang, R., Zheng, Y., Walter, T. R., Weng, H. & Li, J., 2014. Overlapping post-seismic deformation processes: afterslip and viscoelastic relaxation following the 2011 Mw 9.0 Tohoku (Japan) earthquake, *Geophys. J. Int.*, **196**(1), 218–229.
- Dixon, J. E., Dixon, T. H., Bell, D. R. & Malservisi, R., 2004. Lateral variation in upper mantle viscosity: role of water, *Earth planet. Sci. Lett.*, **222**(2), 451–467.
- Dixon, T. H., Jiang, Y., Malservisi, R., McCaffrey, R., Voss, N., Protti, M. & Gonzalez, V., 2014. Earthquake and tsunami forecasts: relation of slow slip events to subsequent earthquake rupture, *Proc. Natl. Acad. Sci.*, **111**(48), 17039–17044.
- Drewes, H. & Heidbach, O., 2012. The 2009 horizontal velocity field for South America and the Caribbean, in *Geodesy for Planet Earth*, Vol. **136**, pp. 657–664, eds Kenyon, S., Pacino, M. C. & Marti, U., Springer Berlin Heidelberg.
- Driscoll, T. A., 2002. *Schwarz-Christoffel Mapping*, 1st edn, Cambridge Univ. Press.
- Dziewonski, A. M. & Anderson, D. L., 1981. Preliminary reference Earth model, *Phys. Earth planet. Inter.*, **25**(4), 297–356.
- Fouedjio, F. & Séguret, S., 2016. Predictive geological mapping using closed-form non-stationary covariance functions with locally varying anisotropy: case study at El Teniente Mine (Chile), *Nat. Resour. Res.*, **25**(4), 431–443.
- Freed, A. M., Hashima, A., Becker, T. W., Okaya, D. A., Sato, H. & Hatanaka, Y., 2017. Resolving depth-dependent subduction zone viscosity and afterslip from postseismic displacements following the 2011 Tohoku-oki, Japan earthquake, *Earth planet. Sci. Lett.*, **459**, 279–290.
- Fujiwara, T., Kodaira, S., No, T., Kaiho, Y., Takahashi, N. & Kaneda, Y., 2011. The 2011 Tohoku-Oki Earthquake: displacement reaching the trench axis, *Science*, **334**(6060), 1240–1240.
- Fukuda, J. & Johnson, K. M., 2021. Bayesian inversion for a stress-driven model of afterslip and viscoelastic relaxation: method and application to postseismic deformation following the 2011 MW 9.0 Tohoku-Oki earthquake, *J. geophys. Res.*, **126**(5), e2020JB021620, doi:10.1029/2020JB021620.
- Furlong, K. P. & Govers, R., 1999. Ephemeral crustal thickening at a triple junction: the Mendocino crustal conveyor, *Geology*, **27**(2), 127–130.
- Gabriel, E. et al., 2004. Open MPI: goals, concept, and design of a next generation MPI implementation, in *Recent Advances in Parallel Virtual Machine and Message Passing Interface*, Vol. **3241**, pp. 97–104, eds Kranzlmüller, D., Kacsuk, P. & Dongarra, J., Springer Berlin Heidelberg.
- Gagnon, K., Chadwell, C. D. & Norabuena, E., 2005. Measuring the onset of locking in the Peru–Chile trench with GPS and acoustic measurements, *Nature*, **434**(7030), 205–208.
- Gahalaut, V. K. et al., 2008. GPS measurements of postseismic deformation in the Andaman-Nicobar region following the giant 2004 Sumatra-Andaman earthquake, *J. geophys. Res.*, **113**(B8), doi:10.1029/2007JB005511.
- Genrich, J. F., Bock, Y., McCaffrey, R., Prawirodirdjo, L., Stevens, C. W., Puntodewo, S. S. O., Subarya, C. & Wdowinski, S., 2000a. Distribution of slip at the northern Sumatran fault system, *J. geophys. Res.*, **105**(B12), 28 327–28 341.
- Gerya, T. V. & Meilick, F. I., 2011. Geodynamic regimes of subduction under an active margin: effects of rheological weakening by fluids and melts, *J. Metamorph. Geol.*, **29**(1), 7–31.
- Geuzaine, C. & Remacle, J.-F., 2009. Gmsh: a 3-D finite element mesh generator with built-in pre- and post-processing facilities, *Int. J. Numer. Methods Eng.*, **79**(11), 1309–1331.
- Govers, R., Furlong, K. P., van de Wiel, L., Herman, M. W. & Broerse, T., 2018. The geodetic signature of the earthquake cycle at subduction zones: model constraints on the deep processes, *Rev. Geophys.*, **56**(1), 6–49.
- Govers, R. & Wortel, R., 1993. Initiation of asymmetric extension in continental lithosphere, *Tectonophysics*, **223**(1), 75–96.
- Govers, R. & Wortel, R., 2005. Lithosphere tearing at STEP faults: response to edges of subduction zones, *Earth planet. Sci. Lett.*, **236**(1), 505–523.
- Haberland, C., Bohm, M. & Asch, G., 2014. Accretionary nature of the crust of Central and East Java (Indonesia) revealed by local earthquake travel-time tomography, *J. Asian Earth Sci.*, **96**, 287–295.
- Hackl, M., Malservisi, R. & Wdowinski, S., 2009. Strain rate patterns from dense GPS networks, *Nat. Hazards Earth Syst. Sci.*, **9**(4), 1177–1187.
- Hall, R., Clements, B. & Smyth, H. R., 2009. Sundaland: basement character, structure and plate tectonic development, in *Proceedings of the 33rd Annual Convention of Indonesian Petroleum Association*, 5–7 May 2009, Jakarta, Indonesia.
- Hall, R. & Sevastjanova, I., 2012. Australian crust in Indonesia, *Aust. J. Earth Sci.*, **59**(6), 827–844.
- Hardebeck, J. L., 2015. Stress orientations in subduction zones and the strength of subduction megathrust faults, *Science*, **349**(6253), 1213–1216.
- Hashimoto, C., Noda, A., Sagiya, T. & Matsu'ura, M., 2009. Interplate seismogenic zones along the Kuril–Japan trench inferred from GPS data inversion, *Nat. Geosci.*, **2**(2), 141–144.
- Hayes, G. P., Moore, G. L., Portner, D. E., Hearne, M., Flamme, H., Furtney, M. & Smoczyk, G. M., 2018. Slab2, a comprehensive subduction zone geometry model, *Science*, **362**(6410), 58–61.
- Herman, M. W. & Govers, R., 2020. Locating fully locked asperities along the South America subduction megathrust: a new physical interseismic inversion approach in a bayesian framework, *Geochem. Geophys. Geosyst.*, **21**(8), doi:10.1029/2020GC009063.
- Herman, Matthew W., Furlong, Kevin P. & Govers, Rob 2018. The Accumulation of Slip Deficit in Subduction Zones in the Absence of Mechanical Coupling: Implications for the Behavior of Megathrust Earthquakes, *Journal of Geophysical Research: Solid Earth*, **123**(8), 8260–8278.
- Hetland, E. A. & Hager, B. H., 2005. Postseismic and interseismic displacements near a strike-slip fault: a two-dimensional theory for general linear viscoelastic rheologies, *J. geophys. Res.*, **110**(B10), doi:10.1029/2005JB003689.
- Hirth, G. & Kohlstedt, D. L., 1996. Water in the oceanic upper mantle: implications for rheology, melt extraction and the evolution of the lithosphere, *Earth planet. Sci. Lett.*, **144**(1), 93–108.
- Hu, Y., Bürgmann, R., Uchida, N., Banerjee, P. & Freymueller, J. T., 2016. Stress-driven relaxation of heterogeneous upper mantle and time-dependent afterslip following the 2011 Tohoku earthquake, *J. geophys. Res.*, **121**(1), 385–411.
- Hu, Y. & Wang, K., 2012. Spherical-Earth finite element model of short-term postseismic deformation following the 2004 Sumatra earthquake, *J. geophys. Res.*, **117**(B5), doi:10.1029/2012JB009153.
- Hutchison, C. S., 1994. Gondwana and Cathaysian blocks, palaeotethys sutures and cenozoic tectonics in South-east Asia, in *Active Continental Margins—Present and Past*, pp. 388–405, eds Giese, P. & Behrmann, J., Springer.
- Hutchison, C. S., 2014. Tectonic evolution of Southeast Asia, *Bull. Geol. Soc. Malaysia*, **60**, 1–18.
- Ikari, M. J., Marone, C. & Saffer, D. M., 2011. On the relation between fault strength and frictional stability, *Geology*, **39**(1), 83–86.
- Itoh, Y., Nishimura, T., Wang, K. & He, J., 2021. New megathrust locking model for the Southern Kurile Subduction Zone incorporating viscoelastic relaxation and non-uniform compliance of upper plate, *J. geophys. Res.*, **126**(5), e2020JB019981, doi:10.1029/2020JB019981.

- Itoh, Y., Wang, K., Nishimura, T. & He, J., 2019. Compliant volcanic arc and backarc crust in Southern Kurile suggested by interseismic geodetic deformation, *Geophys. Res. Lett.*, **46**(21), 11 790–11 798.
- Jin, S. & Park, P.-H., 2006. Strain accumulation in South Korea inferred from GPS measurements, *Earth, Planets Space*, **58**(5), 529–534.
- Jordan, T. E., Isacks, B. L., Allmendinger, R. W., Brewer, J. A., Ramos, V. A. & Ando, C. J., 1983. Andean tectonics related to geometry of subducted Nazca plate, *Bull. geol. Soc. Am.*, **94**(3), 341–361.
- Kanamori, H., 1972. Mechanism of tsunami earthquakes, *Phys. Earth planet. Inter.*, **6**(5), 346–359.
- Karig, D. E., 1974. Evolution of arc systems in the Western Pacific, *Annu. Rev. Earth planet. Sci.*, **2**(1), 51–75.
- Katsumata, K., Wada, N. & Kasahara, M., 2006. Three-dimensional P and S wave velocity structures beneath the Hokkaido corner, Japan-Kurile arc-arc junction, *Earth, Planets Space*, **58**(8), e37–e40.
- Kawakatsu, H., Kumar, P., Takei, Y., Shinohara, M., Kanazawa, T., Araki, E. & Suyehiro, K., 2009. Seismic evidence for sharp lithosphere-asthenosphere boundaries of oceanic plates, *Science*, **324**(5926), 499–502.
- Kellogg, J. N., Vega, V., Stailings, T. C., Aiken, C. L. V. & Kellogg, J. N., 1995. Tectonic development of Panama, Costa Rica, and the Colombian Andes: constraints from Global Positioning System geodetic studies and gravity, *Geol. Soc. Am. Spec. Paper*, **295**, 75–90.
- Kendrick, E., Bevis, M., Smalley, R. & Brooks, B., 2001. An integrated crustal velocity field for the central Andes, *Geochem. Geophys. Geosyst.*, **2**(11), doi:10.1029/2001GC000191.
- Kendrick, E., Brooks, B. A., Bevis, M., Smalley, R., Jr, Lauria, E., Araujo, M. & Parra, H., 2006. Active orogeny of the south-central Andes studied with GPS geodesy, *Revista de La Asociación Geológica Argentina*, **61**(4), 555–566.
- Khazaradze, G. & Klotz, J., 2003. Short- and long-term effects of GPS measured crustal deformation rates along the south central Andes, *J. geophys. Res.*, **108**(B6), doi:10.1029/2002JB001879.
- Kirby, S. H., 1983. Rheology of the lithosphere, *Rev. Geophys.*, **21**(6), 1458–1487.
- Kita, S., Nakajima, J., Hasegawa, A., Okada, T., Katsumata, K., Asano, Y. & Kimura, T., 2014. Detailed seismic attenuation structure beneath Hokkaido, northeastern Japan: arc-arc collision process, arc magmatism, and seismotectonics, *J. geophys. Res.*, **119**(8), 6486–6511.
- Klein, E., Fleitout, L., Vigny, C. & Garaud, J. D., 2016. Afterslip and viscoelastic relaxation model inferred from the large-scale post-seismic deformation following the 2010 Mw 8.8 Maule earthquake (Chile), *Geophys. J. Int.*, **205**(3), 1455–1472.
- Klein, E., Métois, M., Meneses, G., Vigny, C. & Delorme, A., 2018. Bridging the gap between North and Central Chile: insight from new GPS data on coupling complexities and the Andean sliver motion, *Geophys. J. Int.*, **213**(3), 1924–1933.
- Klotz, J., Khazaradze, G., Angermann, D., Reigber, C., Perdomo, R. & Cifuentes, O., 2001. Earthquake cycle dominates contemporary crustal deformation in Central and Southern Andes, *Earth planet. Sci. Lett.*, **193**(3), 437–446.
- Koulali, A. et al., 2017. The kinematics of crustal deformation in Java from GPS observations: implications for fault slip partitioning, *Earth planet. Sci. Lett.*, **458**, 69–79.
- Kreemer, C., Blewitt, G. & Klein, E. C., 2014. A geodetic plate motion and global strain rate model, *Geochem. Geophys. Geosyst.*, **15**(10), 3849–3889.
- Kumar, P. & Kawakatsu, H., 2011. Imaging the seismic lithosphere-asthenosphere boundary of the oceanic plate, *Geochem. Geophys. Geosyst.*, **12**(1), doi:10.1029/2010GC003358.
- Li, S., Bedford, J., Moreno, M., Barnhart, W. D., Rosenau, M. & Oncken, O., 2018. Spatiotemporal variation of mantle viscosity and the presence of cratonic mantle inferred from 8 years of postseismic deformation following the 2010 Maule, Chile, earthquake, *Geochem. Geophys. Geosyst.*, **19**(9), 3272–3285.
- Li, S., Fukuda, J. & Oncken, O., 2020. Geodetic evidence of time-dependent viscoelastic interseismic deformation driven by megathrust locking in the Southwest Japan Subduction zone, *Geophys. Res. Lett.*, **47**(4), doi:10.1029/2019GL085551.
- Li, S., Moreno, M., Bedford, J., Rosenau, M. & Oncken, O., 2015. Revisiting viscoelastic effects on interseismic deformation and locking degree: a case study of the Peru-North Chile subduction zone, *J. geophys. Res.*, **120**(6), 4522–4538.
- Lin, Y. N. et al., 2013. Coseismic and postseismic slip associated with the 2010 Maule Earthquake, Chile: characterizing the Arauco Peninsula barrier effect, *J. geophys. Res.*, **118**(6), 3142–3159.
- Liu, X., Zhao, D. & Li, S., 2013. Seismic heterogeneity and anisotropy of the southern Kuril arc: insight into megathrust earthquakes, *Geophys. J. Int.*, **194**(2), 1069–1090.
- Liu, Z., Owen, S., Dong, D., Lundgren, P., Webb, F., Hetland, E. & Simons, M., 2010. Estimation of interplate coupling in the Nankai trough, Japan using GPS data from 1996 to 2006, *Geophys. J. Int.*, **181**(3), 1313–1328.
- Loveless, J. P. & Meade, B. J., 2010. Geodetic imaging of plate motions, slip rates, and partitioning of deformation in Japan, *J. geophys. Res.*, **115**(B2), doi:10.1029/2008JB006248.
- Loveless, J. P. & Meade, B. J., 2011. Spatial correlation of interseismic coupling and coseismic rupture extent of the 2011 MW = 9.0 Tohoku-oki earthquake, *Geophys. Res. Lett.*, **38**(17), doi:10.1029/2011GL048561.
- Machuca-Mory, D. F. & Deutsch, C. V., 2013. Non-stationary geostatistical modeling based on distance weighted statistics and distributions, *Math. Geosci.*, **45**(1), 31–48.
- Mainprice, D. H. & Paterson, M. S., 1984. Experimental studies of the role of water in the plasticity of quartzites, *J. geophys. Res.*, **89**(B6), 4257–4269.
- Malservisi, R. et al., 2015. Multiscale postseismic behavior on a megathrust: the 2012 Nicoya earthquake, Costa Rica, *Geochem. Geophys. Geosyst.*, **16**(6), 1848–1864.
- MATLAB., 2018. *R2018b*, The MathWorks Inc., Natick, MA.
- Matsu'ura, M. & Sato, T., 1989. A dislocation model for the earthquake cycle at convergent plate boundaries, *Geophys. J. Int.*, **96**(1), 23–32.
- McFarland, P. K., Bennett, R. A., Alvarado, P. & DeCelles, P. G., 2017. Rapid geodetic shortening across the eastern Cordillera of NW Argentina observed by the Puna-Andes GPS array, *J. geophys. Res.*, **122**, 8600–8623.
- McKenzie, K. A. & Furlong, K. P., 2021. Isolating non-subduction-driven tectonic processes in Cascadia, *Geosci. Lett.*, **8**(1), 10.
- Melosh, H. J. & Raefsky, A., 1981. A simple and efficient method for introducing faults into finite element computations, *Bull. seism. Soc. Am.*, **71**(5), 1391–1400.
- Melosh, H. J. & Raefsky, A., 1983. Anelastic response of the Earth to a dip slip earthquake, *J. geophys. Res.*, **88**(B1), 515–526.
- Melosh, H. J. & Williams, C. A., 1989. Mechanics of graben formation in crustal rocks: a finite element analysis, *J. geophys. Res.*, **94**(B10), 13 961–13 973.
- Meltzner, A. J. et al., 2010. Coral evidence for earthquake recurrence and an A.D. 1390–1455 cluster at the south end of the 2004 Aceh–Andaman rupture, *J. geophys. Res.*, **115**(B10), doi:10.1029/2010JB007499.
- Metcalfe, I., 2000. The Bentong–Raub suture zone, *J. Asian Earth Sci.*, **18**(6), 691–712.
- Metcalfe, I., 2011. Tectonic framework and Phanerozoic evolution of Sundaland, *Gondwana Res.*, **19**(1), 3–21.
- Métivier, L., Altamimi, Z. & Rouby, H., 2020. Past and present ITRF solutions from geophysical perspectives, *Adv. Space Res.*, **65**(12), 2711–2722.
- Métois, M. et al., 2013. Revisiting the North Chile seismic gap segmentation using GPS-derived interseismic coupling, *Geophys. J. Int.*, **194**(3), 1283–1294.
- Métois, M., Socquet, A. & Vigny, C., 2012. Interseismic coupling, segmentation and mechanical behavior of the central Chile subduction zone, *J. geophys. Res.*, **117**(B3), doi:10.1029/2011JB008736.
- Métois, M., Vigny, C. & Socquet, A., 2016. Interseismic coupling, megathrust earthquakes and seismic swarms along the Chilean subduction zone (38°–18° S), *Pure appl. Geophys.*, **173**(5), 1431–1449.
- Métois, M., Vigny, C., Socquet, A., Delorme, A., Morvan, S., Ortega, I. & Valderas-Bermejo, C.-M., 2014. GPS-derived interseismic coupling on the subduction and seismic hazards in the Atacama region, Chile, *Geophys. J. Int.*, **196**(2), 644–655.

- Michel, G. W. *et al.*, 2001. Crustal motion and block behaviour in SE-Asia from GPS measurements, *Earth planet. Sci. Lett.*, **187**(3), 239–244.
- Moore, J. C. & Saffer, D., 2001. Updip limit of the seismogenic zone beneath the accretionary prism of southwest Japan: an effect of diagenetic to low-grade metamorphic processes and increasing effective stress, *Geology*, **29**(2), 183–186.
- Moreno, M. *et al.*, 2012. Toward understanding tectonic control on the Mw 8.8 2010 Maule Chile earthquake, *Earth planet. Sci. Lett.*, **321–322**, 152–165.
- Moreno, M., Rosenau, M. & Oncken, O., 2010. 2010 Maule earthquake slip correlates with pre-seismic locking of Andean subduction zone, *Nature*, **467**(7312), 198–202.
- Mouthereau, F., Watts, A. B. & Burov, E., 2013. Structure of orogenic belts controlled by lithosphere age, *Nat. Geosci.*, **6**(9), 785–789.
- Muto, J., Moore, J. D. P., Barbot, S., Iinuma, T., Ohta, Y. & Iwamori, H., 2019. Coupled afterslip and transient mantle flow after the 2011 Tohoku earthquake, *Sci. Adv.*, **5**(9), eaaw1164. doi:
- Nishimura, T., 2011. Back-arc spreading of the northern Izu–Ogasawara (Bonin) Islands arc clarified by GPS data, *Tectonophysics*, **512**(1–4), 60–67.
- Nocquet, J.-M. *et al.*, 2014. Motion of continental slivers and creeping subduction in the northern Andes, *Nat. Geosci.*, **7**(4), 287–291.
- Nocquet, J.-M. *et al.*, 2017. Supercycle at the Ecuadorian subduction zone revealed after the 2016 Pedernales earthquake, *Nat. Geosci.*, **10**(2), 145–149.
- Norabuena, E., Leffler-Griffin, L., Mao, A., Dixon, T., Stein, S., Sacks, I. S., Ocola, L. & Ellis, M., 1998. Space geodetic observations of Nazca–South America convergence across the Central Andes, *Science*, **279**(5349), 358–362.
- Nostro, C., Piersanti, A., Antonioli, A. & Spada, G., 1999. Spherical versus flat models of coseismic and postseismic deformations, *J. geophys. Res.*, **104**(B6), 13 115–13 134.
- Ohzono, M. *et al.*, 2011. Strain accumulation process around the Atotsugawa fault system in the Niigata–Kobe Tectonic Zone, central Japan, *Geophys. J. Int.*, **184**(3), 977–990.
- Ortiz, A. & Zambrano, J. J., 1981. La provincia geológica Precordillera Oriental, *Actas*, **3**, 59–74.
- Pearson, D. M., Kapp, P., DeCelles, P. G., Reiners, P. W., Gehrels, G. E., Duca, M. N. & Pullen, A., 2013. Influence of pre-andean crustal structure on cenozoic thrust belt kinematics and shortening magnitude: northwestern Argentina, *Geosphere*, **9**(6), 1766–1782.
- Perarnau, M., Gilbert, H., Alvarado, P., Martino, R. & Anderson, M., 2012. Crustal structure of the Eastern Sierras Pampeanas of Argentina using high frequency local receiver functions, *Tectonophysics*, **580**, 208–217.
- Pérez-Gussinyé, M., Lowry, A. R., Morgan, J. P. & Tassara, A., 2008. Effective elastic thickness variations along the Andean margin and their relationship to subduction geometry, *Geochem. Geophys. Geosyst.*, **9**(2), doi:10.1029/2007GC001786.
- Pérez-Gussinyé, M., Lowry, A. R. & Watts, A. B., 2007. Effective elastic thickness of South America and its implications for intracontinental deformation, *Geochem. Geophys. Geosyst.*, **8**(5), doi:10.1029/2006GC001511.
- Petit, C. & Fournier, M., 2005. Present-day velocity and stress fields of the Amurian Plate from thin-shell finite-element modelling, *Geophys. J. Int.*, **160**(1), 357–369.
- Pollitz, F. F. *et al.*, 2011b. Coseismic slip distribution of the February 27, 2010 Mw 8.8 Maule, Chile earthquake, *Geophys. Res. Lett.*, **38**(9), doi:10.1029/2011GL047065.
- Pollitz, F. F., Thatcher, W. R. & Hearn, E. H., 2010. The resolution of mantle viscosity using nine years of GPS measurements following the 1999 M = 7.1 Hector Mine, CA, earthquake (Invited), in *AGU Fall Meeting 2010*, abstract id. T51F-02.
- Pollitz, F., Bürgmann, R. & Banerjee, P., 2011a. Geodetic slip model of the 2011 M9.0 Tohoku earthquake, *Geophys. Res. Lett.*, **38**(7), doi:10.1029/2011GL048632.
- Prawirodirdjo, L. *et al.*, 1997. Geodetic observations of interseismic strain segmentation at the Sumatra Subduction Zone, *Geophys. Res. Lett.*, **24**(21), 2601–2604.
- Prawirodirdjo, L., McCaffrey, R., Chadwell, C. D., Bock, Y. & Subarya, C., 2010. Geodetic observations of an earthquake cycle at the Sumatra subduction zone: role of interseismic strain segmentation, *J. geophys. Res.*, **115**(B3), doi:10.1029/97GL52691.
- Protti, M. *et al.*, 2014. Nicoya earthquake rupture anticipated by geodetic measurement of the locked plate interface, *Nat. Geosci.*, **7**(2), 117–121.
- Qiu, Q., Moore, J. D. P., Barbot, S., Feng, L. & Hill, E. M., 2018. Transient rheology of the Sumatran mantle wedge revealed by a decade of great earthquakes, *Nat. Commun.*, **9**(1), doi:10.1038/s41467-018-03298-6.
- Ramos, V. A., 1988. Late proterozoic–early Paleozoic of South America—a collisional history, *Episodes: J. Int. Geosci.*, **11**(3), 168–174.
- Ramos, V. A., 1999. Plate tectonic setting of the Andean Cordillera, *Episodes: J. Int. Geosci.*, **22**(3), 183–190.
- Ranalli, G., 1995. *Rheology of the Earth*, Chapman & Hall.
- Rebischung, P., Griffiths, J., Ray, J., Schmid, R., Collilieux, X. & Garayt, B., 2012. IGS08: the IGS realization of ITRF2008, *GPS Solut.*, **16**(4), 483–494.
- Rivas, C., Ortiz, G., Alvarado, P., Podesta, M. & Martin, A., 2019. Modern crustal seismicity in the northern Andean Precordillera, Argentina, *Tectonophysics*, **762**, 144–158.
- Ruegg, J. C. *et al.*, 2009. Interseismic strain accumulation measured by GPS in the seismic gap between Constitución and Concepción in Chile, *Phys. Earth planet. Inter.*, **175**(1), 78–85.
- Sagiya, T., Miyazaki, S. & Tada, T., 2000. Continuous GPS array and present-day crustal deformation of Japan, *Pure appl. Geophys.*, **157**(11), 2303–2322.
- Satake, K., 2015. Geological and historical evidence of irregular recurrent earthquakes in Japan, *Phil. Trans. R. Soc., A*, **373**(2053), doi:10.1098/rsta.2014.0375.
- Savage, J. C., 1983. A dislocation model of strain accumulation and release at a subduction zone, *J. geophys. Res.*, **88**(B6), 4984–4996.
- Scholz, C. H., 1998. Earthquakes and friction laws, *Nature*, **391**(6662), 37–42.
- Sébrier, M., Mercier, J. L., Macharé, J., Bonnot, D., Cabrera, J. & Blanc, J. L., 1988. The state of stress in an overriding plate situated above a flat slab: the Andes of central Peru, *Tectonics*, **7**(4), 895–928.
- Seemüller, W., Sánchez, L., Seitz, M. & Drewes, H., 2010. The position and velocity solution SIR10P01 of the IGS Regional Network Associate Analysis Centre for SIRGAS (IGS RNAAC SIR). DGFI, Munich, Retrieved from http://www.sirgas.org/fileadmin/docs/SIR10P01_DGFI.Report.86.pdf
- Seno, T., Sakurai, T. & Stein, S., 1996. Can the Okhotsk Plate be discriminated from the North American plate?, *J. geophys. Res.*, **101**(B5), 11305–11315.
- Shestakov, N. V. *et al.*, 2011. Present tectonics of the southeast of Russia as seen from GPS observations: present tectonics of the southeast of Russia, *Geophys. J. Int.*, **184**(2), 529–540.
- Shi, F., Li, S. & Moreno, M., 2020. Megathrust locking and viscous mantle flow induce continental shortening in Central Andes, *Pure appl. Geophys.*, **177**(6), 2841–2852.
- Shi, X., Kirby, J., Yu, C., Jiménez-Díaz, A. & Zhao, J., 2017. Spatial variations in the effective elastic thickness of the lithosphere in Southeast Asia, *Gondwana Res.*, **42**, 49–62.
- Sibson, R., 1981. A brief description of natural neighbour interpolation, *Interpreting Multivariate Data*. Retrieved from <https://ci.nii.ac.jp/naid/10022185042/>
- Simons, M. *et al.*, 2011. The 2011 magnitude 9.0 Tohoku–Oki earthquake: mosaicking the megathrust from seconds to centuries, *Science*, **332**(6036), 1421–1425.
- Simons, W. J. F. *et al.*, 2007. A decade of GPS in Southeast Asia: resolving Sundaland motion and boundaries, *J. geophys. Res.*, **112**(B6), doi:10.1029/2005JB003868.
- Sladen, A. & Trevisan, J., 2018. Shallow megathrust earthquake ruptures betrayed by their outer-trench aftershocks signature, *Earth planet. Sci. Lett.*, **483**, 105–113.
- Stewart, J. & Watts, A. B., 1997. Gravity anomalies and spatial variations of flexural rigidity at mountain ranges, *J. geophys. Res.*, **102**(B3), 5327–5352.

- Styron, R. & Pagani, M., 2020. The GEM Global Active Faults Database, *Earthq. Spectra*, **36**(Suppl 1), 160–180.
- Sun, T. et al., 2014. Prevalence of viscoelastic relaxation after the 2011 Tohoku-oki earthquake, *Nature*, **514**(7520), 84–87.
- Suwa, Y., Miura, S., Hasegawa, A., Sato, T. & Tachibana, K., 2006. Interplate coupling beneath NE Japan inferred from three-dimensional displacement field, *J. geophys. Res.*, **111**(B4), doi:10.1029/2004JB003203.
- Tanaka, A., Yamano, M., Yano, Y. & Sasada, M., 2004. Geothermal gradient and heat flow data in and around Japan (I): appraisal of heat flow from geothermal gradient data, *Earth, Planets Space*, **56**(12), 1191–1194.
- Tatsumi, Y., Otofujii, Y.-I., Matsuda, T. & Nohda, S., 1989. Opening of the Sea of Japan back-arc basin by asthenospheric injection, *Tectonophysics*, **166**(4), 317–329.
- Tichelaar, B. W. & Ruff, L. J., 1993. Depth of seismic coupling along subduction zones, *J. geophys. Res.*, **98**(B2), 2017–2037.
- Tong, X. et al., 2010. The 2010 Maule, Chile earthquake: downdip rupture limit revealed by space geodesy, *Geophys. Res. Lett.*, **37**(24), doi:10.1029/2010GL045805.
- Trubienko, O., Fleitout, L., Garaud, J.-D. & Vigny, C., 2013. Interpretation of interseismic deformations and the seismic cycle associated with large subduction earthquakes, *Tectonophysics*, **589**, 126–141.
- Ueda, H., Ohtake, M. & Sato, H., 2003. Postseismic crustal deformation following the 1993 Hokkaido Nansei-oki earthquake, northern Japan: evidence for a low-viscosity zone in the uppermost mantle, *J. geophys. Res.*, **108**(B3), doi:10.1029/2002JB002067.
- van Keken, P. E., Kiefer, B. & Peacock, S. M., 2002. High-resolution models of subduction zones: implications for mineral dehydration reactions and the transport of water into the deep mantle, *Geochem. Geophys. Geosyst.*, **3**(10), doi:10.1029/2001GC000256.
- Van Veen, B. A. D., Vatvani, D. & Zijl, F., 2014. Tsunami flood modelling for Aceh & west Sumatra and its application for an early warning system, *Cont. Shelf Res.*, **79**, 46–53.
- Veloza, G., Styron, R., Taylor, M. & Mora, A., 2012. Open-source archive of active faults for northwest South America, *GSA Today*, **22**(10), 4–10.
- Verfürth, R., 1994. A posteriori error estimation and adaptive mesh-refinement techniques, *J. Comput. Appl. Math.*, **50**(1), 67–83.
- Vigny, C. et al., 2005. Insight into the 2004 Sumatra–Andaman earthquake from GPS measurements in southeast Asia, *Nature*, **436**(7048), 201–206.
- Vigny, C. et al., 2011. The 2010 Mw 8.8 Maule Megathrust earthquake of Central Chile, monitored by GPS, *Science*, **332**(6036), 1417–1421.
- Villegas-Lanza, J. C., Chlieh, M., Cavalié, O., Tavera, H., Baby, P., Chire-Chira, J. & Nocquet, J.-M., 2016. Active tectonics of Peru: heterogeneous interseismic coupling along the Nazca megathrust, rigid motion of the Peruvian siver, and Subandean shortening accommodation, *J. geophys. Res.*, **121**(10), 7371–7394.
- Voss, N. K., Malservisi, R., Dixon, T. H. & Protti, M., 2017. Slow slip events in the early part of the earthquake cycle, *J. geophys. Res.*, **122**(8), 6773–6786.
- Wackernagel, H., 2003. Ordinary kriging, in *Multivariate Geostatistics: An Introduction with Applications*, pp. 79–88, ed. Wackernagel, H., Springer.
- Wada, I. & Wang, K., 2009. Common depth of slab-mantle decoupling: reconciling diversity and uniformity of subduction zones, *Geochem. Geophys. Geosyst.*, **10**(10), doi:10.1029/2009GC002570.
- Wang, K., Hu, Y., Bevis, M., Kendrick, E., Smalley, R., Jr., Vargas, R. B. & Lauria, E., 2007. Crustal motion in the zone of the 1960 Chile earthquake: detangling earthquake-cycle deformation and forearc-sliver translation, *Geochem. Geophys. Geosyst.*, **8**(10), doi:10.1029/2007GC001721.
- Wang, K., Hu, Y. & He, J., 2012. Deformation cycles of subduction earthquakes in a viscoelastic Earth, *Nature*, **484**(7394), 327–332.
- Wang, K., Zhu, Y., Nissen, E. & Shen, Z.-K., 2021. On the relevance of geodetic deformation rates to earthquake potential, *Geophys. Res. Lett.*, **48**(11), e2021GL093231, doi:10.1029/2021GL093231.
- Wang, M., Li, Q., Wang, F., Zhang, R., Wang, Y., Shi, H., Zhang, P. & Shen, Z., 2011. Far-field coseismic displacements associated with the 2011 Tohoku-oki earthquake in Japan observed by Global Positioning System, *Chinese Sci. Bull.*, **56**(23), 2419–2424.
- Wang, Z. & Zhao, D., 2005. Seismic imaging of the entire arc of Tohoku and Hokkaido in Japan using P-wave, S-wave and sP depth-phase data, *Phys. Earth planet. Inter.*, **152**(3), 144–162.
- Ward, S. N., 1998a. On the consistency of earthquake moment rates, geological fault data, and space geodetic strain: the United States, *Geophys. J. Int.*, **134**(1), 172–186.
- Ward, S. N., 1998b. On the consistency of earthquake moment release and space geodetic strain rates: Europe, *Geophys. J. Int.*, **135**(3), 1011–1018.
- Watts, A. B., 2015. 6.01 - Crustal and lithosphere dynamics: an introduction and overview, in *Treatise on Geophysics*, 2nd edn, pp. 1–44, ed. Schubert, G., Elsevier.
- Watts, A. B., Lamb, S. H., Fairhead, J. D. & Dewey, J. F., 1995. Lithospheric flexure and bending of the Central Andes, *Earth planet. Sci. Lett.*, **134**(1), 9–21.
- Watts, A. B., 1981. The U.S. Atlantic Continental Margin: Subsidence History, Crustal Structure and Thermal Evolution in Bally, Albert W. *Geology of Passive Continental Margins: History, Structure and Sedimentologic Record (with Special Emphasis on the Atlantic Margin)*, American Association of Petroleum Geologists, 1–75.
- Weaver, R., Roberts, A. P., Flecker, R., Macdonald, D. I. M. & Fot'yanova, L. M., 2003. Geodynamic implications of paleomagnetic data from tertiary sediments in Sakhalin, Russia (NW Pacific), *J. geophys. Res.*, **108**(B2), doi:10.1029/2001JB001226.
- Weiss, J. R. et al., 2016. Isolating active orogenic wedge deformation in the southern Subandes of Bolivia, *J. geophys. Res.*, **121**(8), 6192–6218.
- Wessel, P., Luis, J. F., Uieda, L., Scharroo, R., Wobbe, F., Smith, W. H. F. & Tian, D., 2019. The generic mapping tools version 6, *Geochem. Geophys. Geosyst.*, **20**(11), 5556–5564.
- White, S. M., Trenkamp, R. & Kellogg, J. N., 2003. Recent crustal deformation and the earthquake cycle along the Ecuador–Colombia subduction zone, *Earth planet. Sci. Lett.*, **216**(3), 231–242.
- Williams, T. B., Kelsey, H. M. & Freymueller, J. T., 2006. GPS-derived strain in northwestern California: termination of the San Andreas fault system and convergence of the Sierra Nevada–Great Valley block contribute to southern Cascadia forearc contraction, *Tectonophysics*, **413**(3), 171–184.
- Wimpenny, S., Copley, A., Benavente, C. & Aguirre, E., 2018. Extension and dynamics of the Andes inferred from the 2016 Parina (Huarichancara) earthquake, *J. geophys. Res.*, **123**(9), 8198–8228.
- Yamagiwa, S., Miyazaki, S., Hirahara, K. & Fukahata, Y., 2015. Afterslip and viscoelastic relaxation following the 2011 Tohoku-oki earthquake (M_w 9.0) inferred from inland GPS and seafloor GPS/acoustic data, *Geophys. Res. Lett.*, **42**(1), 66–73.
- Yoshioka, S. & Matsuoka, Y., 2013. Interplate coupling along the Nankai Trough, southwest Japan, inferred from inversion analyses of GPS data: effects of subducting plate geometry and spacing of hypothetical ocean-bottom GPS stations, *Tectonophysics*, **600**, 165–174.
- Zhu, Y., Wang, K. & He, J., 2020. Effects of earthquake recurrence on localization of interseismic deformation around locked strike-slip faults, *J. geophys. Res.*, **125**(8), doi:10.1029/2020JB019817.